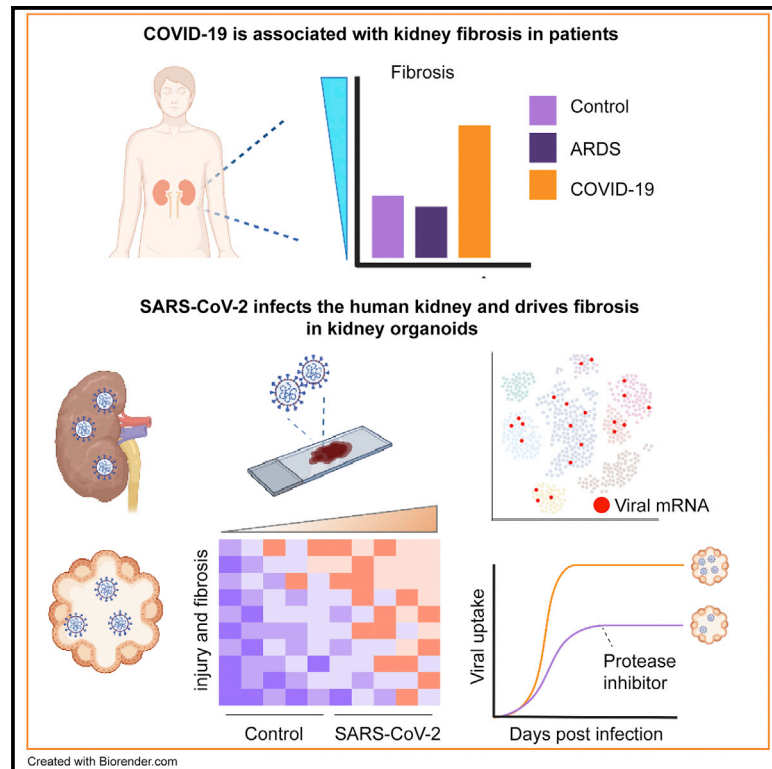# SARS-CoV-2 infects the human kidney and drives fibrosis in kidney organoids

Graphical abstract

Authors

Jitske Jansen, Katharina C. Reimer, James S. Nagai, ..., Rebekka K. Schneider, Bart Smeets, Rafael Kramann

Correspondence

rkramann@gmx.net

In brief

Jansen, Reimer, Nagai, et al. report that SARS-CoV-2 infects kidney cells and is associated with kidney fibrosis in patients. Using single-cell transcriptomics of infected kidney organoids, they show that SARS-CoV-2 causes kidney injury and stimulates profibrotic signaling. Viral infection in organoids was inhibited by a recently developed protease blocker.

Highlights

- COVID-19 patients present tubulo-interstitial kidney fibrosis compared with controls

- SARS-CoV-2 infection stimulates profibrotic signaling in human kidney organoids

- SARS-CoV-2 infection can be inhibited by a protease blocker in human kidney organoids

CellPress

Clinical and Translational Report

SARS-CoV-2 infects the human kidney and drives fibrosis in kidney organoids

Jitske Jansen,[1,2,3,22] Katharina C. Reimer,[1,4,5,22] James S. Nagai,[6,7,22] Finny S. Varghese,[8,23] Gijs J. Overheul,[8]
Marit de Beer,[9] Rona Roverts,[9] Deniz Daviran,[9] Liline A.S. Fermin,[9] Brigith Willemsen,[2] Marcel Beukenboom,[2]
Sonja Djudjaj,[10] Saskia von Stillfried,[10] Larissa E. van Eijk,[11] Mirjam Mastik,[11] Marian Bulthuis,[11] Wilfred den Dunnen,[11]
Harry van Goor,[11] Jan-Luuk Hillebrands,[11] Sergio H. Triana,[12] Theodore Alexandrov,[12,13,14] Marie-Cherelle Timm,[10]
Bartholomeus T. van den Berge,[2,16] Martijn van den Broek,[2,3] Quincy Nlandu,[2] Joelle Heijnert,[2] Eric M.J. Bindels,[15]
Remco M. Hoogenboezem,[15] Fieke Mooren,[2] Christoph Kuppe,[1,4] Pascal Miesen,[8] Katrien Grünberg,[2] Ties Ijzermans,[16]
Eric J. Steenbergen,[2] Jan Czogalla,[17] Michiel F. Schreuder,[3] Nico Sommerdijk,[9] Anat Akiva,[9] Peter Boor,[4,10]
Victor G. Puelles,[17] Jürgen Floege,[4] Tobias B. Huber,[17] The COVID Moonshot consortium, Ronald P. van Rij,[8]
Ivan G. Costa,[6,7,21] Rebekka K. Schneider,[5,18,19,21] Bart Smeets,[2,21] and Rafael Kramann[1,4,20,21,24,*]

[1]Institute of Experimental Medicine and Systems Biology, RWTH Aachen University, Aachen, Germany
[2]Department of Pathology, Radboud Institute for Molecular Life Sciences, Radboud University Medical Center, Nijmegen, the Netherlands
[3]Department of Pediatric Nephrology, Radboud Institute for Molecular Life Sciences, Radboud University Medical Center, Amalia Children's Hospital, Nijmegen, the Netherlands
[4]Division of Nephrology and Clinical Immunology, RWTH Aachen University, Aachen, Germany
[5]Institute for Biomedical Technologies, Department of Cell Biology, RWTH Aachen University, Aachen, Germany
[6]Institute for Computational Genomics, University Hospital RWTH Aachen, Germany
[7]Joint Research Center for Computational Biomedicine, RWTH Aachen University Hospital, Aachen, Germany
[8]Department of Medical Microbiology, Radboud University Medical Center, Radboud Institute for Molecular Life Sciences, Nijmegen, the Netherlands
[9]Electron Microscopy Center, Radboudumc Technology Center Microscopy, Radboud Institute of Molecular Life Sciences, Radboud University Medical Center, Geert Grooteplein, 6525 GA Nijmegen, the Netherlands
[10]Department of Pathology and Electron Microscopy Facility, RWTH Aachen University, Aachen, Germany
[11]Department of Pathology and Medical Biology, University of Groningen, University Medical Center Groningen, Groningen, the Netherlands
[12]Structural and Computational Biology Unit, European Molecular Biology Laboratory, Heidelberg, Germany
[13]Skaggs School of Pharmacy and Pharmaceutical Sciences, University of California, San Diego, La Jolla, CA, USA
[14]Molecular Medicine Partnership Unit (MMPU), European Molecular Biology Laboratory, Heidelberg, Germany
[15]Department of Hematology, Erasmus MC Cancer Institute, Rotterdam, the Netherlands
[16]Department of Nephrology, Radboud Institute for Molecular Life Sciences, Radboud University Medical Center, Nijmegen, the Netherlands
[17]Department of Medicine, University Medical Center Hamburg-Eppendorf, Hamburg, Germany
[18]Department of Developmental Biology, Erasmus Medisch Centrum, Rotterdam, the Netherlands
[19]Oncode Institute, Erasmus Medisch Centrum, Rotterdam, the Netherlands
[20]Department of Internal Medicine, Nephrology and Transplantation, Erasmus Medisch Centrum, Rotterdam, the Netherlands
[21]Senior author
[22]These authors contributed equally
[23]Present address: UniQure N.V., Amsterdam, the Netherlands
[24]Lead contact
*Correspondence: rkramann@gmx.net
https://doi.org/10.1016/j.stem.2021.12.010

SUMMARY

Kidney failure is frequently observed during and after COVID-19, but it remains elusive whether this is a direct effect of the virus. Here, we report that SARS-CoV-2 directly infects kidney cells and is associated with increased tubule-interstitial kidney fibrosis in patient autopsy samples. To study direct effects of the virus on the kidney independent of systemic effects of COVID-19, we infected human-induced pluripotent stem-cell-derived kidney organoids with SARS-CoV-2. Single-cell RNA sequencing indicated injury and dedifferentiation of infected cells with activation of profibrotic signaling pathways. Importantly, SARS-CoV-2 infection also led to increased collagen 1 protein expression in organoids. A SARS-CoV-2 protease inhibitor was able to ameliorate the infection of kidney cells by SARS-CoV-2. Our results suggest that SARS-CoV-2 can directly infect kidney cells and induce cell injury with subsequent fibrosis. These data could explain both acute kidney injury in COVID-19 patients and the development of chronic kidney disease in long COVID.

INTRODUCTION

Severe acute respiratory syndrome coronavirus 2 (SARS-CoV-2) causes an ongoing global pandemic and drives coronavirus disease 2019 (COVID-19). Despite its primary manifestation as a pulmonary disease, evidence substantiates that organs other than the lung are directly affected by SARS-CoV-2 infection. Autopsy studies, case reports, and retrospective clinical studies contributed to a better understanding of the clinical picture of COVID-19. SARS-CoV-2 has been shown to fuel a multitude of pathologies, ranging from neurological symptoms to a higher risk of acute-on-chronic liver failure, altered hemostasis causing venous thromboembolisms, and acute kidney injury (AKI) (Lamers et al., 2020; Piñeiro et al., 2021; Qiu et al., 2020; Wichmann et al., 2020). AKI leads to increased morbidity and mortality, especially in patients with severe underlying conditions treated in an intensive care setting requiring renal replacement therapy (Hoste et al., 2015). In that respect, a clinical study found that 21.4% of COVID-19 patients admitted into intensive care treatment developed AKI stage 2 or higher according to the acute kidney injury network (AKIN) classification (Piñeiro et al., 2021). Possible targets and facilitators for SARS-CoV-2 to bind, infect, and replicate in human cells are the cell-membrane-bound receptor angiotensin-converting enzyme 2 (ACE2), the transmembrane protease serine subtype 2 (TMPRSS2), Furin, and Basigin (BSG, also known as CD147) (Hoffmann et al., 2020; Örd et al., 2020; Wang et al., 2020). The expression of ACE2, TMPRSS2, Furin, and CD147 is not lung-specific, and their presence in a variety of tissues, including the brain, the intestine, and the kidney, could subject these organs to direct infection by SARS-CoV-2 (Donoghue et al., 2000; Lamers et al., 2020; Muramatsu, 2016; Pellegrini et al., 2020; Puelles et al., 2020; Zang et al., 2020). Various recent publications clearly point toward infection of different renal cell populations, including proximal tubule (PT) epithelial cells, in COVID-19 patients (Bouquegneau et al., 2021; Braun et al., 2020; Müller et al., 2021; Puelles et al., 2020). It is currently, however, unclear if this infection is of pathophysiologic relevance for the kidney or not. Recent evidence showed that SARS-CoV-2 directly infects and damages kidney cells, although the cellular changes associated with this infection remain unclear (Braun et al., 2020; Puelles et al., 2020). In COVID-19 patients, AKI could be either a severe complication of the acute respiratory distress syndrome (ARDS) with intensive care treatment, a consequence of the direct infection of kidney cells, or a combination of both. We here demonstrate that SARS-CoV-2 infects podocytes and tubular epithelium in human kidneys and is associated with kidney injury and fibrosis, which can explain the development of chronic kidney disease (CKD) after COVID-19 (Bowe et al., 2021). To study the direct effect of SARS-CoV-2 on the kidney, we infected human-induced pluripotent-stem-cell (iPSC)-derived kidney organoids with SARS-CoV-2, harnessing the advantage of this model system to exclude systemic effects of the disease or renal effects of intensive care medicine treatment. Our data indicate that SARS-CoV-2 infection results in cellular injury and causes activation of multiple profibrotic signaling pathways mediated by cellular crosstalk of infected epithelium and podocytes with interstitial fibroblasts.

RESULTS AND DISCUSSION

SARS-CoV-2 infects kidney cells and is associated with tubule-interstitial fibrosis

To study the effects of SARS-CoV-2 on the kidney, we collected kidney tissue of 62 COVID-19 patients (61 autopsy specimens and 1 biopsy; clinical characteristics are outlined in Table S1). The SARS-CoV-2 nucleocapsid protein was present in the cytoplasm of proximal tubular (PT) epithelium expressing ACE2 (Figures 1A–1F and S1A–S1D), whose localization is in line with previous reports (Diao et al., 2021; Lamers et al., 2020; McBride et al., 2014). SARS-CoV-2 infected lung tissue was used as positive control for the nucleocapsid protein staining (Figure S1E), and non-COVID-19 autopsy and nephrectomy tissues were used as negative controls (Figures 1G and S1F–S1H). PT injury was shown by kidney injury molecule 1 (KIM1) expression in the lotus tetragonolobus lectin (LTL) positive tubules of the biopsy specimen (Figure 1H, negative control Figure 1I). In addition, we observed KIM1 expression in some PTs of COVID-19 patient autopsy kidney tissue (Figures S1I–S1M). Independent of the type of injury, the kidney's response to injury ultimately leads to fibrosis, which is the hallmark of CKD (Duffield, 2014). Interestingly, we observed increased interstitial fibrosis in the kidneys of COVID-19 patients compared with a control cohort that was matched for age, sex, and comorbidities (n = 57) (Figures 1L–1O; clinical characteristics outlined in Table S1). Masson's Trichrome staining and quantitative collagen expression in kidney tissue of all patients revealed significantly elevated levels of extracellular matrix (ECM) in COVID-19 patients' kidneys compared with that of the control cohort (Figure 1M). The control cohort included n = 14 ICU-treated ARDS patients, partially caused by influenza virus infection, of which 71% had AKI. When comparing the COVID-19 cohort to this cohort, we observed increased matrix deposition in the kidneys of COVID-19 patients (Figure 1M). Furthermore, restricting the analysis to control and COVID-19 patients without pre-existing CKD, hypertension, and diabetes confirmed increased matrix deposition in kidneys of COVID-19 patients (Figure 1N). Additionally, subdividing the cohort into patients with and without the presence of CKD prior to the COVID-19 diagnosis indicated increased collagen expression independent of the presence of CKD (Figure 1O). Altogether, these results suggest that SARS-CoV-2 can infect kidney cells and might directly cause kidney injury with subsequent tubule-interstitial fibrosis.

Single-nucleus RNA sequencing shows SARS-CoV-2 infection of renal cells and induction of profibrotic pathways in kidney cells

To further support our finding that SARS-CoV-2 might directly enter and, thus, infect kidney cells, we performed single-nucleus RNA sequencing (snRNA-seq) of autopsy kidney tissue derived from a COVID-19 patient included in our cohort. snRNA-seq revealed 13 distinct cell clusters that were annotated via label-transfer from a recent publicly available kidney snRNA-seq dataset (Muto et al., 2021) (Figures 2A, 2B, and S2A–S2E). The snRNA-seq dataset by Muto et al. from kidney tissue was included as a COVID-19 negative control. To trace SARS-CoV-2 in our dataset, we applied a targeted sequencing approach in combination with a standard 10X Genomics workflow (Triana et al., 2021). After
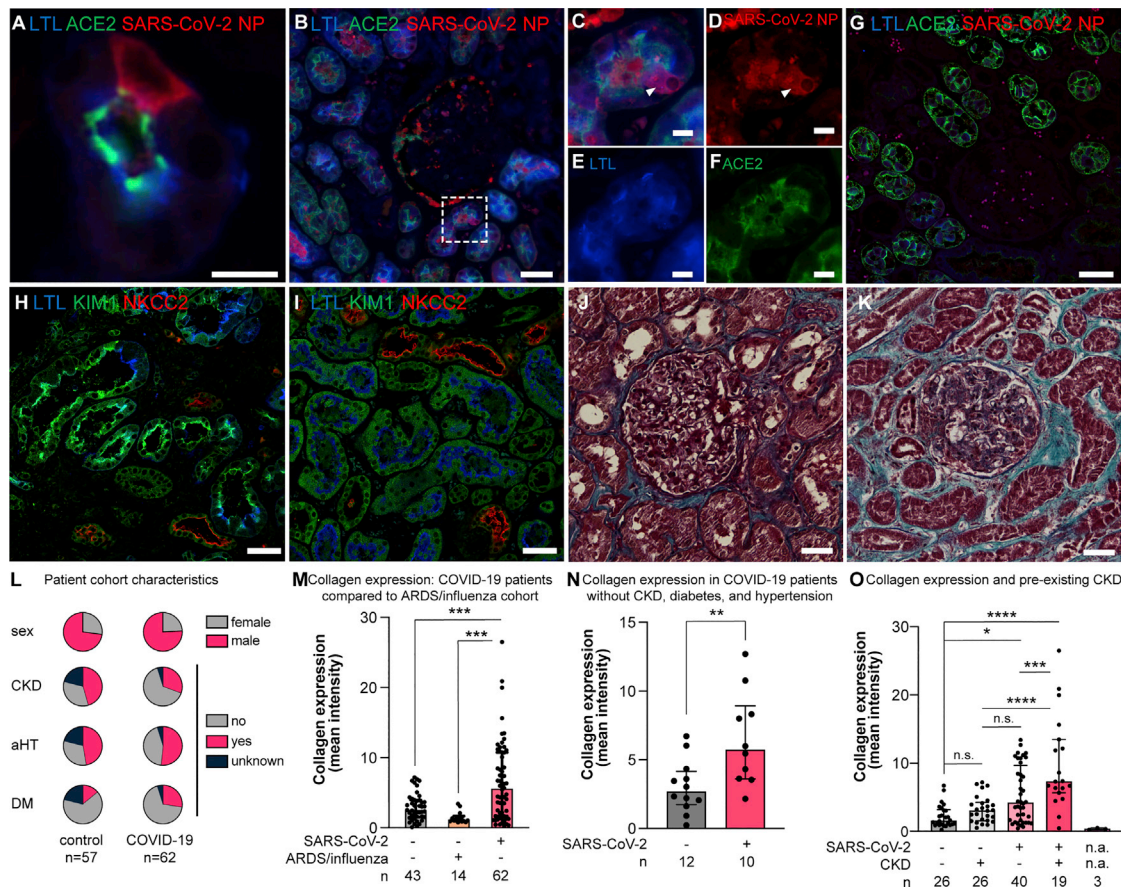
Figure 1. SARS-CoV-2 is present in COVID-19 patient kidney cells and induces fibrosis

(A) SARS-CoV-2 nucleocapsid protein (NP, red, perinuclear), ACE2 (green), and LTL (blue) expression in human COVID-19 kidney biopsy tissue. Scale bars, 10 μm.

(B–G) SARS-CoV-2 NP (B–D, arrowhead, red), ACE2 (B, C, and F, green), and LTL (B, C, and E, blue) expression in human COVID-19 autopsy kidney tissue, (G) autopsy control. Scale bars (C–F), 10 μm.

(H and I) KIM-1 (green), LTL (blue), and NKCC2 (red) expression in human COVID-19 patient kidney biopsy tissue, (I) nephrectomy control.

(K and J) Interstitial fibrosis (collagen fibers in blue) is enhanced in (K) COVID-19 autopsy tissues compared with (J) nephrectomy controls, as quantified based on Masson's trichrome staining.

(L) COVID-19 patient (n = 62) and control cohort (n = 57) characteristics. For details refer to Table S1.

(M) ImageJ quantification of collagen expression in Masson's trichrome-stained COVID-19 patient kidney autopsy tissue compared with control nephrectomy tissue and control ARDS/influenza patient autopsy kidney tissue.

(N) Collagen expression quantification in COVID-19 patient kidney autopsy tissue including patients without CKD, diabetes, and hypertension only.

(O) Comparing COVID-19 patients kidney autopsy tissue with or without pre-existing CKD to respective control cohorts with or without CKD. In Figure S1, representative staining results of other patients included in this study as well as non-COVID-19 autopsy controls are shown. In (M)-(O), data are presented as mean and SD. Scale bars, 50 μm, unless stated otherwise.*p < 0.05, **p < 0.01, ***p < 0.001, ****p < 0.0001. See also Figure S1 and Table S1.

sequencing, we computationally mapped the SARS-CoV-2 reads back to the individual cells. This allowed us to trace viral RNA expression in almost all cell clusters (Figures 2C, 2D, and S2G). Various SARS-CoV-2 entry factors were not present in our dataset, including ACE2, TMPRSS2, BSG, and Furin (Figure S2F) (Hoffmann et al., 2020; Murgolo et al., 2021), likely due to the sparsity of the 3′ sequencing. However, we detected upregulation of the SARS-CoV-2 infection-related genes PLCG2 and AFDN (Delorey et al., 2021). When analyzing ECM remodeling by gene set enrichment analysis (GSEA), we noticed increased collagen, ECM glycoprotein, and proteoglycan expression in COVID-19 kidney tissue fibroblasts compared with the control (Figure 2E). We next applied Pathway RespOnsive GENes for activity inference

(PROGENy), which confirmed increased activity in proinflammatory and fibrosis-driving pathways, including tumor necrosis factor alpha (TNFα), transforming growth factor beta (TGFβ), nuclear factor κB (NFκB), and JAK-STAT, in the COVID-19 patient's PT cells, podocytes, and fibroblasts (Figure 2F). When dissecting cell-cell interactions by CellPhoneDB and CrossTalkeR, PT cells, leukocytes, podocytes, and fibroblasts were among the most active cell types (Figure 2G). Pathways involved in fibrosis-signaling ranked among the top four predominant cell-cell interactions within these clusters (Figure 2H). Signaling from PT cells to fibroblasts revealed in particular fibroblast growth factor receptor (FGFR), EGFR, and platelet-derived growth factor receptor alpha (PDGFRa) signaling to be upregulated (Figure 2I).
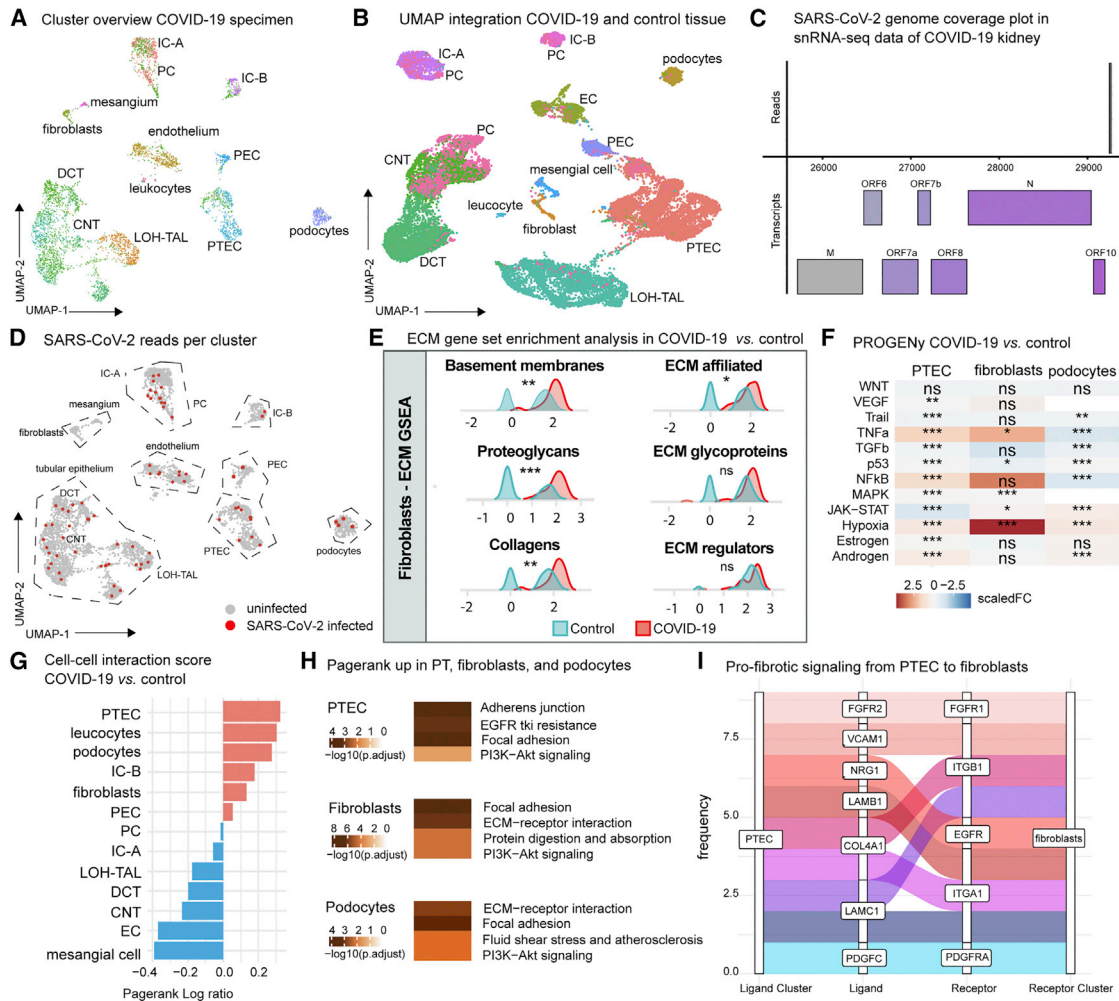
Figure 2. SARS-CoV-2 is present in COVID-19-patient kidney cells on single-cell level and induces ECM remodeling
(A) UMAP overview of clusters detected in snRNA-seq data of one human COVID-19 patient kidney tissue sample.
(B) Integrated UMAP of COVID-19-patient kidney tissue snRNA-seq and control snRNA-seq from a public dataset (Muto et al., 2021).
(C) Coverage plot of the SARS-CoV-2 genome in COVID-19 patient kidney snRNA-seq data.
(D) Targeted sequencing (tapSeq)-based mapping of SARS-CoV-2-containing cells (red dots) per cluster.
(E) Extracellular matrix (ECM) gene set enrichment analysis (GSEA) shows ECM upregulation in COVID-19 versus control kidney snRNA-seq data.
(F) PROGENy pathway analysis reveals fibrosis-related pathway upregulation in COVID-19 versus control snRNA-seq data.
(G) Cell-cell interaction bar plot depicting cell clusters with the highest and lowest interaction scores in COVID-19 versus control kidney snRNA-seq datasets.
(H) Ligand-receptor analysis shows fibrosis-related pathways upregulated in proximal tubular epithelial cells (PTEC), fibroblasts, and podocytes.
(I) Sankey plot illustrating upregulated ligand-receptor interactions from proximal tubular cells to fibroblasts . *p < 0.05, **p < 0.01, ***p < 0.001. See also Figure S2 and Table S2.

These results confirm the direct infection of various human kidney cell types on a single-cell level in autopsy kidney tissue of this COVID-19 patient. Furthermore, these data suggest a potential upregulation of fibrosis-driving pathways and increased renal matrix expression in COVID-19.

SARS-CoV-2 infects proximal tubular cells, podocytes, and stromal cells in iPSC-derived kidney organoids and stimulates collagen I deposition

To study the direct impact of the virus on kidney cells independent of systemic effects, we chose human iPSC-derived kidney organoids to model SARS-CoV-2 infection *in vitro*. Kidney organoids were generated according to an adapted version of the

widely used Little protocol (Takasato et al., 2015) (Figures 3A and 3B). Briefly, iPSCs were differentiated into either ureteric epithelium by exposure to the WNT agonist CHIR 99021 for 3 days or into a metanephric mesenchyme lineage using CHIR 99021 for 5 days. At day 7, cells were mixed in a 1:2 ratio to stimulate morphogenic cues essential for segmented patterning. Organoids were cultured in a 3D air-liquid interface transwell system until day 7+18 before SARS-CoV-2 infection (Figure 3B). The presence of nephron-like structures in our kidney organoids was confirmed by immunofluorescence staining (Figure 3C) as shown by nephrin (podocytes), Lotus tetragonolobus lectin (LTL, PTs) costained with ACE2, which is expressed at the apical side of the proximal tubular cells, similar to human kidneys
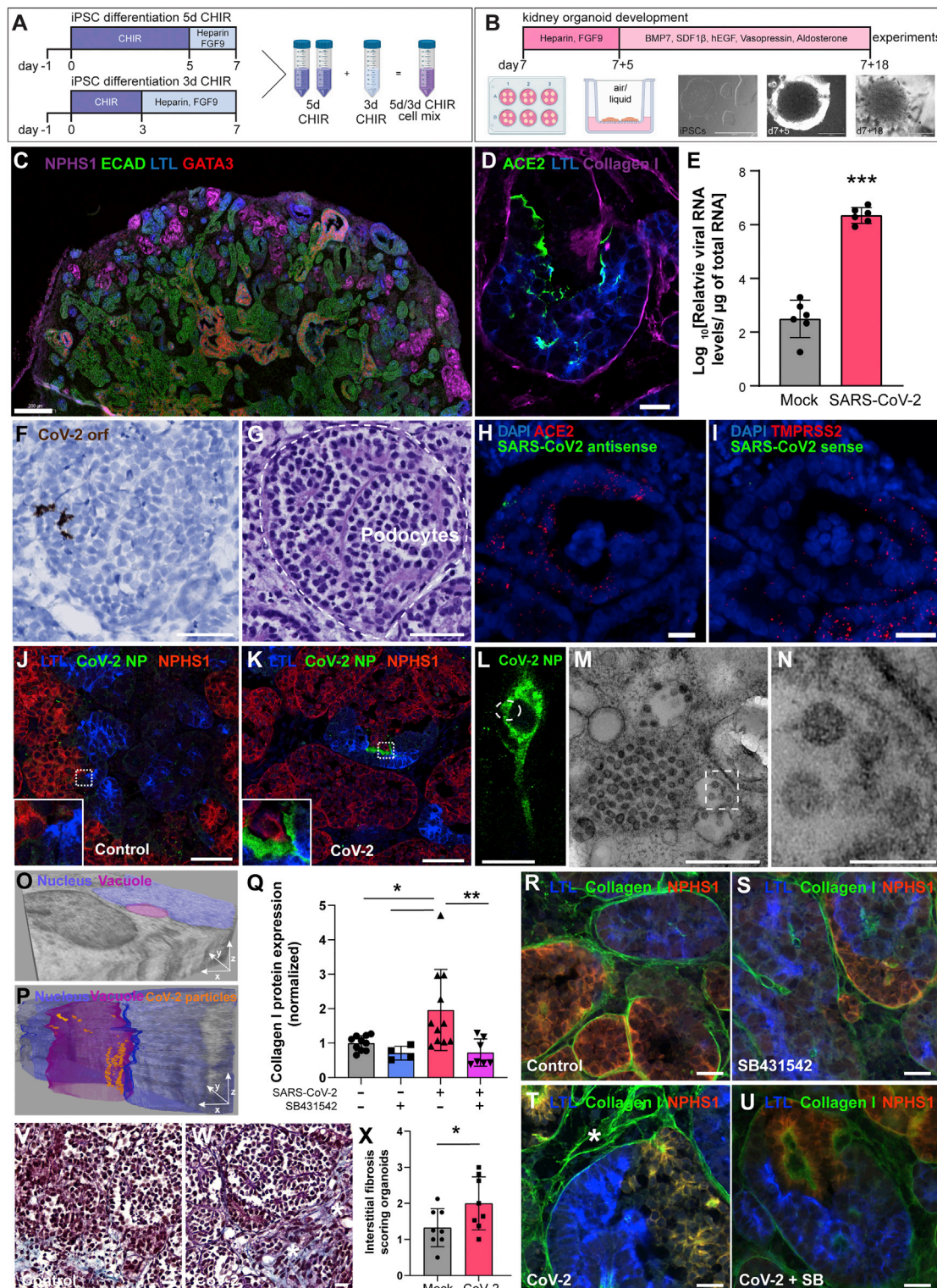
Figure 3. SARS-CoV-2 infects human iPSC-derived kidney organoid cells and stimulates ECM deposition

(A and B) Schematic illustration of the iPSC-derived kidney organoids culture.

(C) Segmented patterning in human kidney organoids shows the presence of podocytes (NPHS1, purple), proximal tubules (LTL, blue), distal-like (ECAD, green), and collecting duct-like (ECAD plus GATA3 [red] costaining) structures. Scale bars, 200 μm.

(D) ACE2 protein expression (green) is present in organoid proximal tubules (LTL, blue). Scale bars, 20 μm.

(legend continued on next page)

(Figure 3D) (The Human Protein Atlas, 2015), E-cadherin (distal-like tubular epithelium), and E-cadherin plus GATA3 (collecting duct-like cells) expression. Organoids were inoculated with SARS-CoV-2 virus particles on day 7+18. The infection was confirmed by viral RNA expression in organoids (Figures 3E and S3A). Using *in situ* hybridization, we confirmed SARS-CoV-2 mRNA expression in podocytes (Figures 3F–3G) and in proximal tubular epithelium (ACE2$^+$, TMPRSS2$^+$, Figures 3H and 3I). Staining of SARS-CoV-2 nucleocapsid protein expression was detected in PTs (Figures 3J, 3K, and S3B–S3D), podocytes (Figures S3B and S3C), and stromal cells (Figure 3L). Next, using immune-based correlative light and electron microscopy (CLEM), we detected viral particles on an ultrastructural level based on the corresponding SARS-CoV-2 nucleocapsid protein fluorescent signal. TEM successfully identified the ultrastructure of viral particles (60–70 nm in diameter) exclusively in SARS-CoV-2 nucleocapsid protein fluorescent positive mesenchymal cells (Figures 3L–3N and S3E–S3L). Notably, we observed viral particles in vacuoles (Figures S3K and S3L), which is in line with the study by Hopfer et al. showing that assembled virions are only present within vacuoles (Hopfer et al., 2021). Using 3D FIB-SEM, we showed the distribution of 65 viral particles in z-dimension throughout a vacuole in close proximity to the nucleus (Figures 3O and 3P). These data indicate that SARS-CoV-2 indeed directly infects human kidney epithelial cells including the stromal compartment.

To verify our results from the COVID-19 patient cohort showing renal fibrosis, we investigated if SARS-CoV-2 infection may contribute to fibrosis in kidney organoids. Quantification of collagen I immunostaining showed increased collagen 1 protein expression in SARS-CoV-2-infected organoids compared with controls (Figures 3Q, 3R, and 3T). TGFβ signaling is a known hallmark of fibrosis (Kramann et al., 2013), and we had seen increased TGFβ signaling in infected renal PT epithelial cells and podocytes in the COVID-19 patient tissue. Hence, we asked whether pharmacologic inhibition of TGFβ signaling could ameliorate SARS-CoV-2-induced fibrosis. The SARS-CoV-2-induced collagen 1 protein expression could indeed be ameliorated by pharmacologically blocking the TGFβ receptor I using

SB431542 (Figures 3Q–3U). In addition to collagen 1 protein expression analysis, we used Masson's Trichrome staining, which is the widely used gold standard technique to image and quantify fibrosis (Kramann et al., 2015a, 2015b; LeBleu et al., 2013). SARS-CoV-2-infected organoids showed increased fibrosis compared with control organoids, as shown by Masson's Trichrome quantification (Figures 3V–3X). These results suggest a cytopathological response after SARS-CoV-2 infection in kidney organoids that may contribute to fibrosis development.

Single-cell RNA sequencing of human iPSC-derived kidney organoids confirms infection of proximal tubular epithelium and podocytes

In order to further analyze the changes in cellular composition and signaling in response to SARS-CoV-2 infection, we performed single-cell RNA sequencing (scRNA-seq) of control and SARS-CoV-2-infected iPSC-derived kidney organoids. We were able to computationally retrieve data from more than 27,000 high-quality cells with 15 distinct cell populations in both infected and noninfected kidney organoids (Figures 4A and S4A–S4D). The cell types included podocytes, proximal tubular cells, loop of Henle progenitor cells (LP cells), mesenchyme cluster 1 (containing endothelial cell progenitors (CD34^{+-} ETS1$^+$EMCN$^+$), and PDGFRa/b$^+$ fibroblasts (Figures S4E–S4I), the latter known to be the key source of myofibroblast (Kuppe et al., 2021), mesenchyme cluster 2, and off-target cells (neural cells 1–5, neural progenitor (NP) cells, and muscle cells 1–4; Phipson et al., 2019), with the majority of the cells being in the G1 phase (Figure 4B). The top differentially expressed (DE) genes per cluster showed known cell-type-specific marker genes for the reported cell populations including EPCAM and KRT18 for proximal tubular cells; NPHS2 and PODXL for podocytes; COL3A1, PDGFRA, and PITX2 for mesenchymal cells; TOP2A, UBE2C, and HMGB2 for loop progenitor cells; MSX1, STMN2, CRABP1, and NEUROD1 for neural cells and their progenitors; and ACTC1, TTN, TNNC2, and MYLPF in muscle cells (Figures 4C and 4D; Table S3). PT cells also express LRP2, ABCC4, and SLC22A5, which have been reported to be specific

---

(E) COVID-19 viral RNA detection in infected kidney organoids. For the mock infection, the same type of medium was used as that in which virus was propagated and added as the same percentage as in the virus-infected organoids. Data are given as mean and SD from 3 independent experiments each performed with 2 biological replicates. ***p $\leq$ 0.001.

(F) mRNA transcript expression of SARS-CoV-2 open reading frame (ORF, brown stain, arrow heads) in podocytes using BROWN Assay *In Situ* Hybridization (BRISH). Scale bars, 50 μm.

(G) Periodic acid-Schiff stain of the BRISH positive podocyte cluster shown in (F). Scale bars, 50 μm.

(H and I) (H) mRNA transcript expression of ACE2, SARS-CoV-2 antisense, and (I) TMPRSS2 in proximal tubules using FISH. Scale bars, 20 μm.

(J and K) SARS-CoV-2 nucleocapsid protein detection (green) in proximal tubules (LTL, blue) in (J) mock-infected and (K) infected kidney organoids. Scale bars, 50 μm.

(L–N) Immuno-based correlative light and electron microscopy (CLEM) analysis of a (L) SARS-CoV-2 nucleocapsid protein-positive mesenchymal cell. Scale bars, 10 μm.

(M and N) TEM ultrastructure analysis of viral particles (60–70 nm) in the corresponding SARS-CoV-2 nucleocapsid protein-positive mesenchymal cell as shown in (L). (M) Scale bars, 500 nm; (N) scale bars, 100 nm. In Figure S3, the sequential CLEM workflow of a cell of interest is shown.

(O and P) 3D FIB-SEM segmentation showing viral particles (orange) in a vacuole (magenta) in close proximity to the nucleus (blue). In (O), a total volume of 5 × 7 × 1.7 μm^3 is shown. Voxel size: 5 nm.

(P) 3D reconstruction of the stack presented in (O). The vacuole (purple) dimensions are ∼2 × 1 × 1.7 μm^3.

(Q–U) Collagen I expression quantification of (R) mock, (S) SB431542 (10 μM), (T) SARS-CoV-2 (* increased collagen I [green]), and (U) SARS-CoV-2 plus SB431542-treated organoids. Scale bars, 20 μm. Data are mean and SD from five independent experiments, each performed with two biological replicates, of which two experiments were supplemented with the TGFb inhibitor SB431542 (10 μM). *p < 0.05, **p < 0.01.

(V–X) Masson's trichrome staining of (V) mock and (W) SARS-CoV-2-infected organoids (* collagenous extracellular matrix, [blue]), (X) quantification. Scale bars, 20 μm. Data are given as mean and SD from four independent experiments each performed with two biological replicates. *p < 0.05. See also Figure S3.
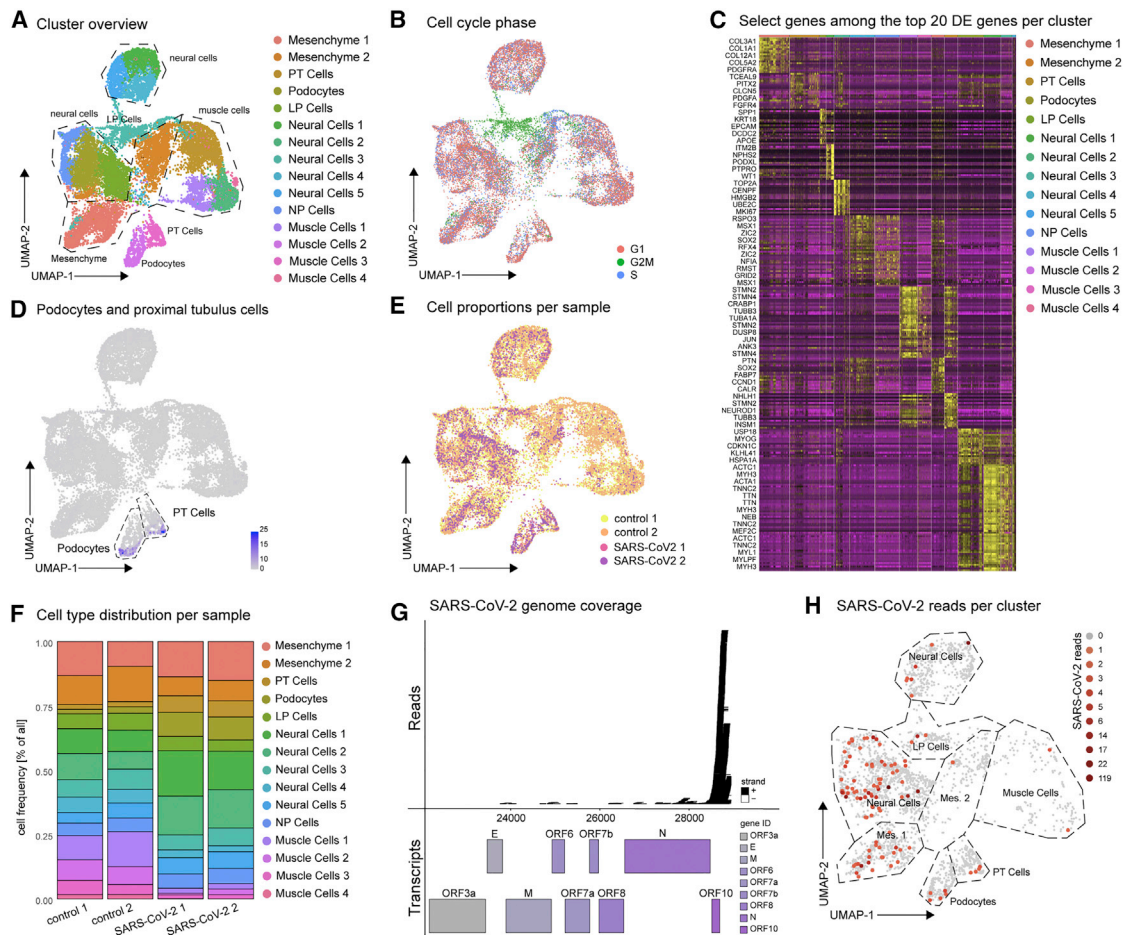
Figure 4. Single-cell-level resolution reveals 15 distinct cell clusters and detection of the SARS-CoV-2 genome in SARS-CoV-2-infected human iPSC-derived kidney organoids

(A) UMAP integration of 27,754 single cells of human iPSC-derived kidney organoids results in 15 different cell clusters: mesenchyme 1, mesenchyme 2, PT (proximal tubule) cells, podocytes, LP (loop progenitor) cells, 6 neural cell clusters (neural cells 1–5 and NP [neural progenitor] cells), and 4 muscle cell clusters (muscle cells 1–4).

(B) UMAP visualization of cell cycle phases. Cells in phase G1 are illustrated in red, those in G2M stage in green, and S-phase cells in blue.

(C) Heatmap illustrating a selection of the top 20 differentially expressed (DE) genes per cluster. The full list of the top 20 DE genes per cluster corresponding to this heatmap is available in Table S3.

(D) UMAP depicting proximal tubule cells (PT cells) and podocytes by marker genes (both populations are highlighted by black dashed lines; PT cells marker genes: EPCAM, KRT18, LRP2 [top 119], ABCC4 [top 201], and SLC22A5 [top 416]; podocyte marker genes: NPHS2 and PODXL). Gray dots represent all non-PT and nonpodocyte cells.

(E) Cell proportion analysis of the 2 mock-infected and 2 SARS-CoV-2-infected samples.

(F) scRNA sequencing of control and SARS-CoV-2-infected iPSC-derived kidney organoids resulted in the illustrated cell-type distribution per sample. In all four samples, we could identify 15 distinct cell populations (mesenchyme 1, mesenchyme 2, PT (proximal tubule) cells, podocytes, LP (loop progenitor) cells, 6 neural cell clusters (neural cells 1–5 and NP [neural progenitor] cells), and 4 muscle cell clusters (muscle cells 1–4).

(G) Coverage plot of reads aligned to the SARS-CoV-2 genome in infected sample 2 (The respective plot for sample 1 is found in Figure S4K).

(H) SARS-CoV-2 reads per single cell per cluster. The color gradient ranges from gray (0 reads per cell) to dark red (119 reads per cell). An overview of viral reads and number of infected cells per cluster and sample is shown in Table S4. See also Figure S4 and Tables S3 and S4.

PT marker genes (El-Achkar et al., 2021; Soo et al., 2018). While we observed an overall higher cell capture in control samples, the 15 cell clusters were present in all four samples (Figure 4E). The cell-type distribution between the control and the SARS-CoV-2-infected kidney organoid samples was overall similar, particularly for replicates. However, the infected kidney organoids displayed a larger percentage of neural cells (neural cells 2 and 3, and NP cells), and podocytes, and less muscle cells (muscle cells 1–3) than the controls (Figure 4F). While ACE2,

TMPRSS2, and Furin expression are not detectable in our dataset, the SARS-CoV-2 entry factor BSG was expressed in, among others, mesenchymal clusters, podocytes, and proximal tubular epithelium (Figure S4J). Furthermore, we identified upregulation of PLCG2 and AFDN upon SARS-CoV-2 infection in nearly all cell clusters. The upregulation of these genes was previously reported in the human COVID-19 tissue atlas, in which COVID-19 patient kidneys and various other organs were mapped using scRNA-seq (Delorey et al., 2021). To further dissect and quantify

SARS-CoV-2-infected cells within the infected samples, we applied a computational method to detect viral reads in scRNA-seq data (Bost et al., 2020). We mapped the expression of SARS-CoV-2 in the infected samples (Figures 4G and S4K), with the majority of reads locating to the N-gene, the open reading frame (ORF) 10 gene and the 3′ untranslated region of the virus genome. The overall number of cells that showed viral gene expression in the scRNA-seq data was low in both samples, which can partially be explained by the sparsity of the 3′-sequencing (Figure 4G). Similar to previous reports of a neural tropism of SARS-CoV-2 (Jacob et al., 2020), neural cells and their progenitors showed the highest fraction of cells with viral reads detected, but proximal tubular cells, podocytes, and mesenchymal cells also appeared among the top viral read-containing cells (Figure S4L). SARS-CoV-2 gene expression was detected in 4% to 25% of proximal tubular cells and 1.4% to 18% of podocytes (Figures 4H and S4L; Table S4). These data indicate that two important human kidney cell types, namely proximal tubular epithelium and podocytes, can be infected by SARS-CoV-2 in iPSC-derived kidney organoids and confirm our findings in the kidney tissue of COVID-19 patients.

Profibrotic signaling pathways are upregulated in SARS-CoV-2-infected kidney organoids

Next, we examined gene expression profiles and signaling pathways in infected kidney organoids to resolve potential pathophysiological mechanisms induced by SARS-CoV-2 (Figures 5 and S5). In proximal tubular cells and podocytes showing viral transcripts, genes related to antiapoptotic and proinflammatory responses were enriched (i.e., TMSB10, S100A9, HSPA1A, and NR2F1; Figure 5A; Ka et al., 2006; Wang et al., 2011; Wu et al., 2020). In line, the top 10 DE genes associated with viral transcription in the mesenchymal clusters also indicated inflammatory signaling (JUN, CCN1, and NFKBIA) (Figure 5A; Jun and Lau, 2011; Ma et al., 2007; Markó et al., 2016). KEGG pathway analysis comparing control versus SARS-CoV-2-infected organoids demonstrated upregulated TGFβ, PI3K/Akt, MAPK, and WNT signaling in proximal tubular cells and mesenchymal clusters (Figure 5B). These pathways have all been reported to be highly important in the pathogenesis of kidney fibrosis (Kramann et al., 2013). In addition, JAK-STAT signaling was solely upregulated in proximal tubular cells (Figure 5B). All cell clusters of interest (i.e., mesenchyme, proximal tubular cells, podocytes, and loop progenitors) showed a "COVID-19"-upregulated signature indicating virus-induced expression changes (Figure 5B). In line, GO terms pointed toward viral processing in all clusters of interest (Figure S5A). Furthermore, the GO-term "collagen-containing extracellular matrix" was slightly enriched in all clusters, particularly in mesenchyme 1 (Figure S5A). We next applied PROGENy to get more insights into pathway activities (Schubert et al., 2018). The results indicated increased activity of MAPK, NFκB, TNFα, and JAK-STAT in proximal tubular cells as well as MAPK and JAK-STAT pathways in podocytes (Figure 5C). Mesenchyme 1 cells showed increased MAPK, NFκB, TNFα, WNT, and TGFβ activity (Figures 5C and SB5). These pathways have all been reported to play an important role in fibroblast activation and myofibroblast differentiation and support the initiation of an injury response that might drive fibrosis (Henderson et al., 2020; Schunk et al., 2021).

To understand the potential changes in transcriptional regulation, we next applied DoRothEA to infer transcription factor activity from the gene expression data (Garcia-Alonso et al., 2019). We identified increased MYC, E2F4, serum response factor (SRF), JUN, and SP1 activity in proximal tubular cells, podocytes, and mesenchymal cells, which are known to be involved in stress response and profibrotic signaling (Figure 5D) (Ajay et al., 2014; Córdova et al., 2015; Kong et al., 2019; Ma et al., 2007; Shen et al., 2017). We then compared cells in which we could detect viral transcription to cells of the same cluster without detectable viral transcription. This analysis pointed toward upregulation of pathways associated with injury and repair processes in infected proximal tubular cells, podocytes, and mesenchyme 1 (Figures S5C–S5E). As such, oxidative phosphorylation, MYC, mTOR, glycolysis, and TGFβ signaling were upregulated in the infected proximal tubular epithelium. These are known pathways involved in damage response and regeneration (Eymael and Smeets, 2016; Grahammer et al., 2014; Kirita et al., 2020; Tammaro et al., 2020). In podocytes and mesenchyme 1, the top 10 upregulated pathways included TGFβ, mTOR, MYC, and p53 signaling (Figures S5C–S5E). GO terms associated with viral transcription in mesenchyme 1 (the cluster containing PDGFRa/b⁺ kidney fibroblasts) were "extracellular matrix," "collagen-containing extracellular matrix," and several terms that indicated increased ribosomal activity. These findings are all in line with a profibrotic response and early myofibroblast differentiation of these cells (Figures S5F–S5H). In proximal tubular cells, the GO terms "vesicles" and "vacuole membranes" were enriched, suggesting cellular stress and injury (Figure S5F). Vacuolization is frequently observed in PTs following ischemia or nephrotoxic injury (Kaissling et al., 2013). Similarly, in podocytes, a stress response was indicated by the GO terms "actin cytoskeleton" and "focal adhesion" (Figure S5G). The actin cytoskeleton is essential to maintain the complex podocyte morphology and fulfill their function in the glomerular filtration barrier. Cytoskeleton rearrangements disturb cellular homeostasis, leading to podocyte injury and, ultimately, kidney injury (Schell and Huber, 2017).

Altogether, these data suggest that SARS-CoV-2 infection contributes to cellular injury, dedifferentiation, and profibrotic signaling in kidney organoids and thus might give an explanation why COVID-19 is associated with a high risk of AKI and potentially also CKD as a long-term consequence in patients that have recovered from COVID-19.

Ligand-receptor analysis reveals potential fibrosis-driving crosstalk between tubular epithelium and mesenchyme

To decipher intercellular communication that drives profibrotic signaling in SARS-CoV-2-infected organoids, we analyzed ligand-receptor pairs using CellPhoneDB and CrossTalkeR (Figures 5E–5J, S5I, and S5J). This analysis suggested an increased likelihood of cell-cell interactions between proximal tubular cells and the PDGFRa/b⁺ mesenchyme 1 population and also between podocytes and the endothelial cell progenitor population in mesenchyme 1 in SARS-CoV-2-infected organoids compared with controls (Figure 5E). Proximal tubular ligands included the ECM component LAMA1, Notch signaling-associated JAG1, and cell junction regulator AFDN (Figure 5F). Collagen 1 and 4, Laminin C1, Wnt5a, TGFβ, VEGFA, JAG1, and THBS1 were
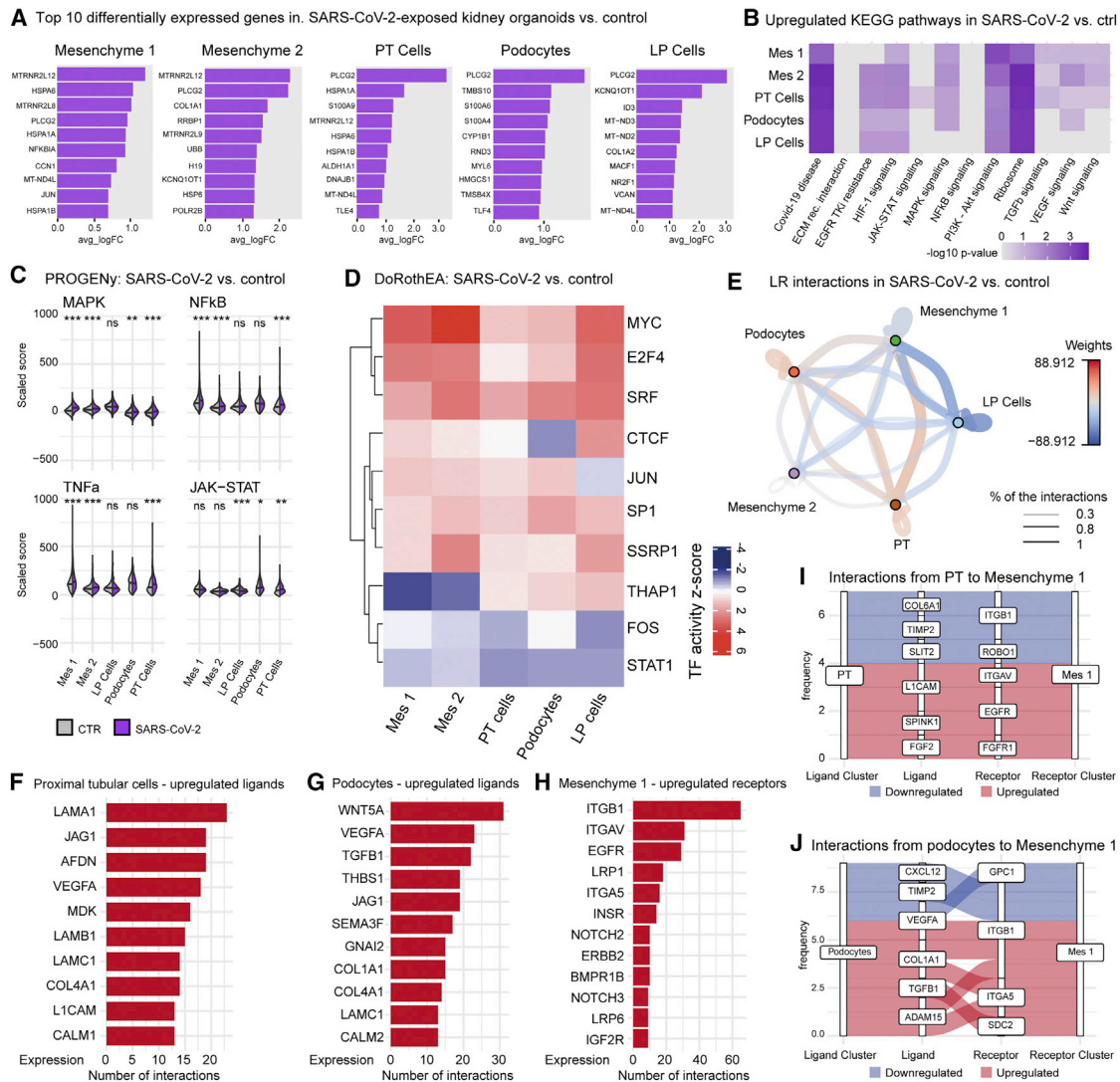
Figure 5. Pathway and ligand-receptor analysis in control versus SARS-CoV-2-infected human iPSC-derived kidney organoids reveal upregulation of fibrosis-related pathways and corresponding cellular crosstalk

(A) Top 10 most prominent genes expressed per mesenchymal (mesenchyme 1 and 2) and kidney cell clusters (PT [proximal tubule] cells, podocytes, and LP [loop progenitor] cells), compared between cells where we could detect viral transcription and cells of the same cluster without detectable viral transcription. Here, we only consider cells from the SARS-CoV-2-infected organoids.

(B) Heatmap illustrating upregulated pathways derived from the KEGG database in control versus SARS-CoV-2-infected human iPSC-derived kidney organoids.

(C) PROGENy violin plots showing selected pathway gene sets in control (gray) versus SARS-CoV-2 (purple)-infected human iPSC-derived kidney organoids. *p < 0.05, **p < 0.01, ***p < 0.001.

(D) DoRothEA heatmap showing upregulated (red) and downregulated (blue) transcription factor activity in control versus SARS-CoV-2-infected human iPSC-derived kidney organoids.

(E) Map of differential cell-cell interaction (CCI) network uncovering cellular crosstalk between select clusters in scRNA sequencing data comparing SARS-CoV-2-infected iPSC-derived kidney organoids to untreated control iPSC-derived kidney organoids.

(F–H) Bar graphs highlighting the top-ranked (F) ligands in proximal tubule cells, (G) podocytes, and (H) receptors in mesenchyme 1 cells.

(I and J) Sankey diagrams showing ligand-receptor pairs between (I) proximal tubule cells and mesenchyme 1 cells and (J) podocytes and mesenchyme 1 cells.
See also Figure S5.

predominant podocyte ligands (Figure 5G). Upregulated receptors for both proximal tubular cells and podocytes mainly included integrins (Figure S5I). Upregulated receptors in mesenchyme 1 contained ITGB1 and ITGAV (both known glomerular endothelial cell receptors; Uhlén et al., 2015), NOTCH, and EGFR (Figure 5H).

The ligand-receptor analysis supports a model in which not only infected tubular epithelial cells but also podocytes might signal to mesenchyme by FGF-FGFR1, TGFβ-SDC2, and COL1A1-ITGA5 (Figures 5I and 5J). All these pathways have been reported as important in profibrotic signaling and could, thus, potentially explain the development of kidney fibrosis
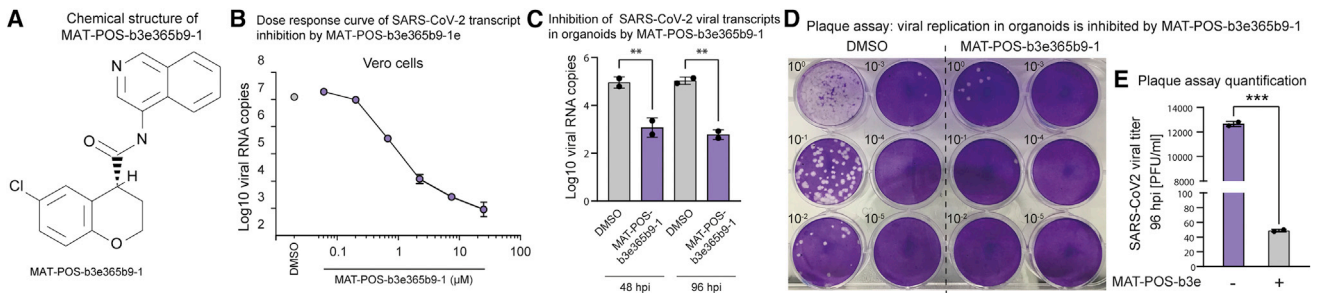
Figure 6. SARS-CoV-2 uptake is inhibited in human iPSC-derived kidney organoids by a protease inhibitor
(A) Chemical structure of MAT-POS-b3e365b9-1.
(B) Dose-response curve in Vero E6 cells infected with SARS-CoV-2 (isolate BavPat1) and treated with the indicated concentrations of MAT-POS-b3e365b9-1 or DMSO at 24 h after infection (hpi). Data are given as mean and SD from two independent experiments.
(C–E) Intracellular viral RNA at 48 and 96 hpi, and (D and E) plaque assay on Vero E6 cells of the apical medium at 96 hpi of kidney organoids infected with SARS-CoV-2 in the presence of 10-μM MAT-POS-b3e365b9-1 or DMSO. Data are given as mean and SD from a representative experiment of two independent experiments, each performed with two biological replicates. Intracellular viral RNA levels in (C) were normalized to expression of the β-actin housekeeping gene. **p < 0.01, ***p < 0.001.

caused by SARS-CoV-2 (Lin et al., 2018; Rayego-Mateos et al., 2018).

SARS-CoV-2 infection in kidney organoids is inhibited by a protease inhibitor
A next step in the combat against SARS-CoV-2 and associated kidney injury would be the prevention of viral uptake by kidney epithelial cells. We tested a noncovalent inhibitor of the SARS-CoV-2 main protease developed by the COVID Moonshot consortium (Chodera et al., 2020; Achdout et al., 2020) (MAT-POS-b3e365b9-1; Figure 6A). This inhibitor effectively reduced intracellular SARS-CoV-2 RNA levels in VeroE6 cells over 4-logs (Figure 6B). Likewise, treatment of kidney organoids with 10 μM of MAT-POS-b3e365b9-1 reduced intracellular viral RNA and infectious virus secretion into the apical compartment over 100-fold (Figures 6C–6E). Therefore, the use of protease inhibitors, as presented here, might potentially be used to reduce SARS-CoV-2 viral replication in kidney cells.

Recent evidence indicates that COVID-19 patients develop AKI and are more likely retain chronic kidney functional impairment after severe disease (Bowe et al., 2020; Hultström et al., 2021). We here demonstrate direct infection of kidney cells in COVID-19 patients, including tubular epithelium, podocytes, and parietal epithelial cells, confirming previous findings (Bouquegneau et al., 2021; Braun et al., 2020; Müller et al., 2021; Omer et al., 2021; Puelles et al., 2020). Furthermore, our data indicate that COVID-19 patients show increased tubule-interstitial fibrosis when comparing their kidney tissue with the tissue of ICU-treated ARDS—due to influenza or other causes—patients or age-matched non-SARS-CoV-2-infected individuals, independent of pre-existing CKD prevalence. This finding may suggest that patients with severe COVID-19 may be at risk of CKD in the future, as kidney fibrosis is a hallmark of CKD (Duffield, 2014). In line with this, using snRNA-seq of a COVID-19 kidney tissue specimen, we showed that kidney epithelial cells were infected and showed enhanced proinflammatory and profibrotic signaling, accompanied by ECM deposition by fibroblasts. Using human iPSC-derived kidney organoids as a model system, we aimed to study the direct effects of SARS-CoV-2 infection, independent of systemic effects of the disease or effects due to ICU treatment, as organoids lack immune cells and fluid flow.

First, we showed that the kidney organoids express SARS-CoV-2 entry factors, such as ACE2 and TMPRSS2, and can be successfully infected with the virus, in line with previous reports (Monteil et al., 2020). We then investigated pathway and cellular interaction profile changes by scRNA-seq. Our findings point toward increased profibrotic signaling, cellular injury, and inflammatory responses driven by SARS-CoV-2 infection of kidney cells. The activated profibrotic signaling cascades in infected organoids and enhanced collagen I protein expression are in line with those of viral infection and fibrotic tissue remodeling seen in COVID-19 patient kidney tissue we present in this study. Our organoid study shows primary pathophysiological effects directly driven by the infection of kidney cells and independent of immune response effects or other systemic impacts, e.g., by blood pressure changes during ARDS with subsequently reduced renal perfusion or pharmacological interventions. Major pathways involved in fibrosis include WNT, EGFR, TGFβ, NOTCH, FGF, Hedgehog, PDGFR, JAK-STAT, and connective tissue growth factor (CTGF) signaling (Kramann et al., 2013). Recent work by our group points toward injured proximal tubular cells being among the strongest cellular crosstalk partners of fibrosis-driving PDGFRa⁺/PDGFRb⁺ myofibroblasts in human CKD (Kuppe et al., 2021). Epithelial to interstitial signaling as an important driver of renal fibrogenesis has been reported in various other studies as well (Bielesz et al., 2010; Maarouf et al., 2016; Zhou et al., 2013). Here, we report that in SARS-CoV-2-infected kidney organoids, FGF, TGFβ, and collagen I signaling from proximal tubular cells and podocytes to mesenchyme cluster 1 (PDGFRa⁺/b⁺), suggests a potential link toward development of fibrosis. This profibrotic signaling as a result of SARS-CoV-2 infection has not been dissected in lung, brain, and intestinal organoid models yet, most likely due to the absence of epithelial-interstitial cellular complexity (Chugh et al., 2021). In lung organoid models, viral infection alongside proinflammatory signatures were observed, while no other pathophysiological signals were detected (Chugh et al., 2021). Infected 3D kidney spheroids, known to lack an interstitial compartment, showed no apparent injury molecules or

fibrosis development (Omer et al., 2021). In the same study, the authors observed increased collagen expression in infected monolayer epithelial cells (Omer et al., 2021). This certainly points toward an injury phenotype of infected epithelial cells, while we and others have demonstrated that epithelial-cell-derived collagen expression does not contribute to fibrosis *in vivo* (Kuppe et al., 2021).

This underlines that more complex multicellular organoids, such as kidney organoids, might aid in resolving pathophysiological crosstalk mechanisms involved in profibrotic signaling, as was also previously shown by Lemos et al. (2018).

While neural cells within our kidney organoids are off-target cells from the differentiation of iPSC toward kidney cell types (Phipson et al., 2019), their increased infectability compared with other cell types is in line with previous studies showing high infection rates of neurons in iPSC-derived brain organoids (Pellegrini et al., 2020), which might partially explain neurological symptoms in patients (e.g., loss of smell and taste).

Taken together, our data show that the direct infection of kidney cells by SARS-CoV-2 lead to a molecular switch toward profibrotic signaling and subsequent tissue injury. Because organoids lack immune cells and perfusion, our data support a model in which kidney injury by SARS-CoV-2 is at least partially independent of systemic effects of the disease or intensive care treatment and rather represents a direct effect of the virus. Thus, virus infection might directly drive acute injury and fibrotic remodeling with subsequent kidney functional decline and CKD.

Limitations of the study

The aim of our study was to investigate the impact of SARS-CoV-2 infection on kidney cells in both COVID-19 patient kidney tissue and a model of human iPSC-derived kidney organoids. Overall, we recovered less cells in the scRNA-seq data of SARS-CoV-2-infected organoid samples (approximately 2,000 cells per sample) than from the controls (around 12,000 cells per sample). A potential explanation could be that due to SARS-CoV-2 infection, the cells might be more susceptible to damage; thus, they might not survive the handling pre-scRNA-seq as well, as numerical cell input was the same for control samples and SARS-CoV-2-infected organoids. Furthermore, using scRNA-seq, we could not detect significant SARS-CoV-2 entry factor expression in the kidney organoid scRNA-seq dataset, while we could detect ACE2 and TMPRSS2 expression in organoids using immunofluorescence staining and ISH. Potentially, the missing expression of ACE2, TMPRSS2, Furin, and BSG in the scRNA-seq data might be due to the sparsity of the 3′ sequencing.

The current state of modeling human kidneys by differentiating iPSCs is a still immature, second-trimester fetal kidney model system that does not fully resemble the adult kidney and contains off-target cell types. In this respect, certain cell populations are spatially differentially distributed compared with the adult kidney. For instance, in the human kidney, podocytes and endothelial cells are in close proximity as they are key components of the glomerular filtration barrier. Signaling between both cell types is essential for proper filtration of the blood. However, in organoids, this adult anatomy is not present yet, and endothelial progenitors are still clustered in the mesenchyme. Thus, the ligand-receptor analysis provided in this study needs to be interpreted in this context. Furthermore, when using iPSC-derived kidney organoids to model

adult human disease, such as COVID-19, the drawbacks of this model system should be considered. This includes an early developmental phenotype compared with the adult kidney, the lack of an immune system, and some off-target cell types. However, iPSC organoids still have several advantages over other models because they represent a three-dimensional human kidney system in the dish that contains many renal compartments and cell types. We have recently demonstrated that iPSC-derived kidney organoids are a useful tool to model kidney fibrosis and to validate therapeutic targets of adult human CKD and fibrosis (Kuppe et al., 2021). While our data provide insights into cellular signaling and crosstalk in kidney cell injury during SARS-CoV-2 infection, the contribution of other factors potentially resulting in AKI in COVID-19, such as ARDS and multiorgan failure, immune effects, age, comorbidities, and ICU treatment, require further investigation. Long-term clinical as well as autopsy studies will be essential to unravel constellations that drive AKI and fibrosis induction in COVID-19 and might contribute to progression toward CKD post COVID-19.

STAR★METHODS

Detailed methods are provided in the online version of this paper and include the following:

- KEY RESOURCES TABLE
- RESOURCE AVAILABILITY
  - Lead contact
  - Materials availability
  - Data and code availability
- EXPERIMENTAL MODEL AND SUBJECT DETAILS
  - Human autopsy, nephrectomy, and biopsy kidney tissue
  - Human induced pluripotent stem cells (iPSCs)
  - Culturing human induced pluripotent stem cell (iPSC) derived kidney organoids
- METHOD DETAILS
  - RNA extraction, cDNA synthesis and viral load analysis
  - Infection of human iPSC-derived kidney organoids with SARS-CoV-2 and treatment with TGFb inhibitor SB431542
  - Blocking SARS-CoV-2 entry into kidney organoid cells by MAT-POS-b3e365b9-1
  - Preparing paraffin sections of human iPSC-derived kidney organoids
  - Fluorescence In Situ Hybridization (FISH)
  - RNAscope 2.5 High Definition (HD) - BROWN Assay In Situ Hybridization
  - Immunofluorescence staining
  - Immuno-based correlative light microscopy and electron microscopy (CLEM)
  - 3D focused ion beam - scanning electron microscopy (FIB-SEM)
  - Preparation of single cell suspensions from iPSC-derived kidney organoids
  - Preparation of single nuclei suspensions from snap-frozen human autopsy kidney tissue
  - Single cell and single nuclei RNA library preparation and sequencing

- ○ Single nuclei RNA seq data analysis of human autopsy kidney tissue
- ○ TAP-Seq single nuclei RNA seq data analysis of human autopsy kidney tissue
- ○ Single cell RNA seq data analysis of human iPSC-derived kidney organoids
- ○ SARS-CoV-2 differential gene expression analysis
- ○ SARS-CoV-2 pathway activity and transcription factor analysis
- ○ Cellular crosstalk
- ○ Discovering viral reads using Viral-Track
- ○ Gene expression analysis of SARS-CoV-2-infected cells
- ● QUANTIFICATIONS AND STATISTICAL ANALYSIS
- ○ Histochemical quantification of collagen
- ○ Quantification of fibrosis within Masson's Trichrome staining in human tissue
- ○ Fibrosis scoring following Masson's Trichrome staining of SARS-CoV-2-infected kidney organoids
- ○ Quantification of SARS-CoV-2 nucleocapsid protein expression in kidney organoids
- ○ Statistical analysis

SUPPLEMENTAL INFORMATION

Supplemental information can be found online at https://doi.org/10.1016/j.stem.2021.12.010.

CONSORTIA

The COVID Moonshot Consortium contributors are Hagit Achdout, Anthony Aimon, Elad Bar-David, Haim Barr, Amir Ben-Shmuel, James Bennett, Melissa L. Boby, Bruce Borden, Gregory R. Bowman, Juliane Brun, Sarma BVNBS, Mark Calmiano, Anna Carbery, Emma Cattermole, Eugene Chernychenko, John D. Choder, Austin Clyde, Joseph E. Coffland, Galit Cohen, Jason Cole, Alessandro Contini, Lisa Cox, Milan Cvitkovic, Alex Dias, Kim Donckers, David L. Dotson, Alica Douangamath, Shirly Duberstein, Tim Dudgeon, Louise Dunnett, Peter K. Eastman, Noam Erez, Charles J. Eyermann, Mike Fairhead, Gwen Fate, Daren Fearon, Oleg Federov, Matteo Ferla, Rafaela S. Fernandes, Lori Ferrins, Richard Foster, Holly Foster, Ronen Gabizon, Adolfo Garcia-Sastre, Victor O. Gawriljuk, Paul Gehrtz, Carina Gileadi, Charline Giroud, William G. Glass, Robert Glen, Itai glinert, Andre S. Godoy, Marian Gorichko, Tyler Gorrie-Stone, Ed J. Griffen, Storm Hassell Hart, Jag Heer, Micheal Henry, Michelle Hill, Sam Horrell, Matthew F.D. Hurley, Tomer Israely, Andrew Jajack, Eric Jnoff, Dirk Jochmans, Tobias John, Steven De Jonghe, Anastassia L. Kantsadi, Peter W. Kenny, J. L. Kiappes, Lizbe Koekemoer, Boris Kovar, Tobias Krojer, Alpha A. Lee, Bruce A. Lefker, Haim Levy, Nir London, Petra Lukacik, Hannah Bruce Macdonald, Beth Maclean, Tika R. Malla, Tatiana Matviiuk, Willam McCorkindale, Briana L. McGovern, Sharon Melamed, Oleg Michurin, Halina Mikolajek, Bruce F. Milne, Aaron Morris, Garret M. Morris, Melody Jane Morwitzer, Demetri Moustakas, Aline M. Nakamura, Jose Brandao Neto, Johan Neyts, Luong Nguyen, Gabriela D. Noske, Vladas Oleinikovas, Glaucius Oliva, Gijs J. Overheul, David Owen, Vladimir Psenak, Ruby Pai, Jin Pan, Nir Paran, Benjamin Perry, Maneesh Pingle, Jakir Pinjari, Boaz Politi, Ailsa Powell, Reut Puni, Victor L. Rangel, Ranbabu N. Reddi, St Patrick Reid, Efrat Resnick, Emily Grace Ripka, Matthew C. Robinson, Ralph P. Robinson, Jaime Rodriguez-Guerra, Romel Rosales, Dominic Rufa, Chris Schofield, Mikhail Shafeev, Aarif Shaikh, Jiye Shi, Khriesto Shurrush, Sukrit Sing, Assa Sittner, Rachael Skyner, Adam Smalley, Mihaela D. Smilova, Leonardo J. Solmesky, John Spencer, Claire Strain-Damarell, Vishwanath Swamy, Hadas Tamir, Rachael Tennant, Warren Thompson, Andrew Thompson, Warren Thompson, Susana Tomasia, Anthony Tumber, Ioannis Vakonakis, Ronald P. van Rij, Laura van Geel, Finny S. Varghese, Mariana Vaschetto, Einat B. Vitner, Vincent Voelz, Andra Volkamer, Frank von Delft, Annette von Delft, Martin Walsh, Walter Ward, Charlie Weatherall, Shay Weiss, Kris M. White,

Conor Francis Wild, Matthew Wittmann, Nathan Wright, Yfat Yahalom-Ronen, Daniel Zaidmann, Hadeer Zidane, and Nicole Zitzmann.

AUTHOR CONTRIBUTIONS

J.J., K.C.R., B.S., R.K.S., and R.K. designed the study. J.J., K.C.R., M.V.D.B., and B.T.V.D.B. cultured the iPSC-derived kidney organoids. T.I., E.J.S., K.G., P.B., S.V.S., V.G.P., J.C., T.B.H., H.V.G., J.-L.H., L.E.v.E., and W.D.D. obtained consent from patients, obtained ethical approvals, and provided tissue specimens. J.J., S.D., M.-C.T., M.V.D.B., B.T.V.D.B., B.W., R.R., M.B., F.M., Q.N., and J.H. performed tissue processing, IF, and trichrome stainings, as well as RNAscope experiments. M.B., R.R., D.D., L.A.S.F., N.S., and A.A. performed CLEM and 3D FIB-SEM analyses. L.E.E., M.M., M.B., W.D., H.G., and J.-L.H contributed tissue specimens and performed BRISH experiments. F.S.V., G.J.O., P.M., and R.P.V.R. designed and carried out SARS-CoV-2 infection experiments of the organoids. F.S.V., G.J.O., P.M., and K.C.R. performed data acquisition experiments for scRNA-seq. C.K. and K.C.R. isolated nuclei and performed data acquisition for snRNA-seq. J.S.N. and I.G.C. carried out the scRNA-seq and snRNA-seq data analyses. S.H.T. and T.A. provided protocols and assisted with tapSeq analysis. J.J., K.C.R., J.S.N., and R.K. wrote the manuscript. J.J., K.C.R., J.S.N., R.P.V.R., R.K.S., R.K., and I.G.C. arranged the figures. R.K.S., B.S., I.G.C., P.B., S.D., S.V.S., M.F.S., B.T.V.D.B, V.G.P., A.A., P.M., R.P.V.R., C.K., and R.K. edited the manuscript and advised on data analysis and interpretation. All authors read and approved the final manuscript.

DECLARATION OF INTERESTS

The authors declare no competing interests.

REFERENCES

Achdout, H., Aimon, A., Bar-David, E., Barr, H., Ben-Shmuel, A., Bennett, J., Bobby, M.L., Brun, J., Sarma, B., et al.; The COVID Moonshot Consortium (2020). COVID moonshot: open science discovery of SARS-CoV-2 main protease inhibitors by combining crowdsourcing, high-throughput experiments, computational simulations, and machine learning. BioRxiv. https://doi.org/10.1101/2020.10.29.339317.

Ajay, A.K., Kim, T.M., Ramirez-Gonzalez, V., Park, P.J., Frank, D.A., and Vaidya, V.S. (2014). A bioinformatics approach identifies signal transducer and activator of transcription-3 and checkpoint kinase 1 as upstream regulators of kidney injury molecule-1 after kidney injury. J. Am. Soc. Nephrol. 25, 105–118.

Alvarez, M.J., Shen, Y., Giorgi, F.M., Lachmann, A., Ding, B.B., Ye, B.H., and Califano, A. (2016). Functional characterization of somatic mutations in cancer using network-based inference of protein activity. Nat. Genet. 48, 838–847.

Bielesz, B., Sirin, Y., Si, H., Niranjan, T., Gruenwald, A., Ahn, S., Kato, H., Pullman, J., Gessler, M., Haase, V.H., and Susztak, K. (2010). Epithelial Notch signaling regulates interstitial fibrosis development in the kidneys of mice and humans. J. Clin. Invest. 120, 4040–4054.

Bost, P., Giladi, A., Liu, Y., Bendjelal, Y., Xu, G., David, E., Blecher-Gonen, R., Cohen, M., Medaglia, C., Li, H., et al. (2020). Host-viral infection maps reveal signatures of severe COVID-19 patients. Cell 181, 1475–1488.e12.

Bouquegneau, A., Erpicum, P., Grosch, S., Habran, L., Hougrand, O., Huart, J., Krzesinski, J.-M., Misset, B., Hayette, M.-P., Delvenne, P., and Bovy, C. (2021). COVID-19–associated nephropathy includes tubular necrosis and capillary congestion, with evidence of SARS-CoV-2 in the nephron. Kidney360 2, 639–652.

Bowe, B., Cai, M., Xie, Y., Gibson, A.K., Maddukuri, G., and Al-Aly, Z. (2020). Acute kidney injury in a national cohort of hospitalized US veterans with COVID-19. Clin. J. Am. Soc. Nephrol. 16, 14–25.

Bowe, B., Xie, Y., Xu, E., and Al-Aly, Z. (2021). Kidney outcomes in long COVID. J. Am. Soc. Nephrol. 32, 2851–2862.

Braun, F., Lütgehetmann, M., Pfefferle, S., Wong, M.N., Carsten, A., Lindenmeyer, M.T., Nörz, D., Heinrich, F., Meißner, K., Wichmann, D., et al. (2020). SARS-CoV-2 renal tropism associates with acute kidney injury. Lancet 396, 597–598.

Butler, A., Hoffman, P., Smibert, P., Papalexi, E., and Satija, R. (2018). Integrating single-cell transcriptomic data across different conditions, technologies, and species. Nat. Biotechnol. 36, 411–420.

Cabello-Aguilar, S., Alame, M., Kon-Sun-Tack, F., Fau, C., Lacroix, M., and Colinge, J. (2020). SingleCellSignalR: inference of intercellular networks from single-cell transcriptomics. Nucleic Acids Res. 48, e55.

Chodera, J., Lee, A.A., London, N., and von Delft, F. (2020). Crowdsourcing drug discovery for pandemics. Nat. Chem. 12, 581.

Chugh, R.M., Bhanja, P., Norris, A., and Saha, S. (2021). Experimental models to study COVID-19 effect in stem cells. Cells 10, 91.

Córdova, G., Rochard, A., Riquelme-Guzmán, C., Cofré, C., Scherman, D., Bigey, P., and Brandan, E. (2015). SMAD3 and SP1/SP3 transcription factors collaborate to regulate connective tissue growth factor gene expression in myoblasts in response to transforming growth factor β. J. Cell. Biochem. 116, 1880–1887.

Corman, V.M., Landt, O., Kaiser, M., Molenkamp, R., Meijer, A., Chu, D.K., Bleicker, T., Brünink, S., Schneider, J., Schmidt, M.L., et al. (2020). Detection of 2019 novel coronavirus (2019-nCoV) by real-time RT-PCR. Euro surveillance: bulletin Europeen sur les maladies transmissibles 25, 2000045.

Delorey, T.M., Ziegler, C.G.K., Heimberg, G., Normand, R., Yang, Y., Segerstolpe, Å., Abbondanza, D., Fleming, S.J., Subramanian, A., Montoro, D.T., et al. (2021). COVID-19 tissue atlases reveal SARS-CoV-2 pathology and cellular targets. Nature 595, 107–113.

Diao, B., Wang, C., Wang, R., Feng, Z., Zhang, J., Yang, H., Tan, Y., Wang, H., Wang, C., Liu, L., et al. (2021). Human kidney is a target for novel severe acute respiratory syndrome coronavirus 2 infection. Nat. Commun. 12, 2506.

Donoghue, M., Hsieh, F., Baronas, E., Godbout, K., Gosselin, M., Stagliano, N., Donovan, M., Woolf, B., Robison, K., Jeyaseelan, R., et al. (2000). A novel angiotensin-converting enzyme-related carboxypeptidase (ACE2) converts angiotensin I to angiotensin 1–9. Circ. Res. 87, E1–E9.

Duffield, J.S. (2014). Cellular and molecular mechanisms in kidney fibrosis. J. Clin. Invest. 124, 2299–2306.

Efremova, M., Vento-Tormo, M., Teichmann, S.A., and Vento-Tormo, R. (2020). CellPhoneDB: inferring cell-cell communication from combined expression of multi-subunit ligand-receptor complexes. Nat. Protoc. 15, 1484–1506.

El-Achkar, T.M., Eadon, M.T., Menon, R., Lake, B.B., Sigdel, T.K., Alexandrov, T., Parikh, S., Zhang, G., Dobi, D., Dunn, K.W., et al. (2021). A multimodal and integrated approach to interrogate human kidney biopsies with rigor and reproducibility: guidelines from the Kidney Precision Medicine Project. Physiol. Genomics 53, 1–11.

Eymael, J., and Smeets, B. (2016). Origin and fate of the regenerating cells of the kidney. Eur. J. Pharmacol. 790, 62–73.

Garcia-Alonso, L., Holland, C.H., Ibrahim, M.M., Turei, D., and Saez-Rodriguez, J. (2019). Benchmark and integration of resources for the estimation of human transcription factor activities. Genome Res. 29, 1363–1375.

Garcia-Alonso, L., Iorio, F., Matchan, A., Fonseca, N., Jaaks, P., Peat, G., Pignatelli, M., Falcone, F., Benes, C.H., Dunham, I., et al. (2018). Transcription factor activities enhance markers of drug sensitivity in cancer. Cancer Res. 78, 769–780.

Grahammer, F., Haenisch, N., Steinhardt, F., Sandner, L., Roerden, M., Arnold, F., Cordts, T., Wanner, N., Reichardt, W., Kerjaschki, D., et al. (2014). mTORC1 maintains renal tubular homeostasis and is essential in response to ischemic stress. Proc. Natl. Acad. Sci. USA 111, E2817–E2826.

Heiligenstein, X., de Beer, M., Heiligenstein, J., Eyraud, F., Manet, L., Schmitt, F., Lamers, E., Lindenau, J., Kea-Te Lindert, M., Salamero, J., et al. (2021). HPM live μ for a full CLEM workflow. Methods Cell Biol 162, 115–149.

Henderson, N.C., Rieder, F., and Wynn, T.A. (2020). Fibrosis: from mechanisms to medicines. Nature 587, 555–566.

Hoffmann, M., Kleine-Weber, H., Schroeder, S., Krüger, N., Herrler, T., Erichsen, S., Schiergens, T.S., Herrler, G., Wu, N.H., Nitsche, A., et al. (2020). SARS-CoV-2 cell entry depends on ACE2 and TMPRSS2 and is blocked by a clinically proven protease inhibitor. Cell 181, 271–280.e8.

Hopfer, H., Herzig, M.C., Gosert, R., Menter, T., Hench, J., Tzankov, A., Hirsch, H.H., and Miller, S.E. (2021). Hunting coronavirus by transmission electron microscopy - a guide to SARS-CoV-2-associated ultrastructural pathology in COVID-19 tissues. Histopathology 78, 358–370.

Hoste, E.A.J., Bagshaw, S.M., Bellomo, R., Cely, C.M., Colman, R., Cruz, D.N., Edipidis, K., Forni, L.G., Gomersall, C.D., Govil, D., et al. (2015). Epidemiology of acute kidney injury in critically ill patients: the multinational AKI-EPI study. Intensive Care Med. 41, 1411–1423.

Hultström, M., Lipcsey, M., Wallin, E., Larsson, I.M., Larsson, A., and Frithiof, R. (2021). Severe acute kidney injury associated with progression of chronic kidney disease after critical COVID-19. Crit. Care 25, 37.

Jacob, F., Pather, S.R., Huang, W.K., Zhang, F., Wong, S.Z.H., Zhou, H., Cubitt, B., Fan, W., Chen, C.Z., Xu, M., et al. (2020). Human pluripotent stem cell-derived neural cells and brain organoids reveal SARS-CoV-2 neurotropism predominates in choroid plexus epithelium. Cell Stem Cell 27, 937–950.e9.

Jun, J.I., and Lau, L.F. (2011). Taking aim at the extracellular matrix: CCN proteins as emerging therapeutic targets. Nat. Rev. Drug Discov. 10, 945–963.

Ka, S.M., Rifai, A., Chen, J.H., Cheng, C.W., Shui, H.A., Lee, H.S., Lin, Y.F., Hsu, L.F., and Chen, A. (2006). Glomerular crescent-related biomarkers in a murine model of chronic graft versus host disease. Nephrol. Dial. Transplant. 21, 288–298.

Kaissling, B., Lehir, M., and Kriz, W. (2013). Renal epithelial injury and fibrosis. Biochim. Biophys. Acta 1832, 931–939.

Kirita, Y., Wu, H., Uchimura, K., Wilson, P.C., and Humphreys, B.D. (2020). Cell profiling of mouse acute kidney injury reveals conserved cellular responses to injury. Proc. Natl. Acad. Sci. USA 117, 15874–15883.

Kolde, R., and Kolde, M.R. (2015). Package "pheatmap. R package 1, 790.

Kong, M., Chen, X., Lv, F., Ren, H., Fan, Z., Qin, H., Yu, L., Shi, X., and Xu, Y. (2019). Serum response factor (SRF) promotes ROS generation and hepatic stellate cell activation by epigenetically stimulating NCF1/2 transcription. Redox Biol. 26, 101302.

Kramann, R., DiRocco, D.P., and Humphreys, B.D. (2013). Understanding the origin, activation and regulation of matrix-producing myofibroblasts for treatment of fibrotic disease. J. Pathol. 231, 273–289.

Kramann, R., Fleig, S.V., Schneider, R.K., Fabian, S.L., DiRocco, D.P., Maarouf, O., Wongboonsin, J., Ikeda, Y., Heckl, D., Chang, S.L., et al. (2015b). Pharmacological GLI2 inhibition prevents myofibroblast cell-cycle progression and reduces kidney fibrosis. J. Clin. Invest. 125, 2935–2951.

Kramann, R., Schneider, R.K., DiRocco, D.P., Machado, F., Fleig, S., Bondzie, P.A., Henderson, J.M., Ebert, B.L., and Humphreys, B.D. (2015a). Perivascular Gli1+ progenitors are key contributors to injury-induced organ fibrosis. Cell Stem Cell 16, 51–66.

Kuppe, C., Ibrahim, M.M., Kranz, J., Zhang, X., Ziegler, S., Perales-Patón, J., Jansen, J., Reimer, K.C., Smith, J.R., Dobie, R., et al. (2021). Decoding myofibroblast origins in human kidney fibrosis. Nature 589, 281–286.

Lamers, M.M., Beumer, J., van der Vaart, J., Knoops, K., Puschhof, J., Breugem, T.I., Ravelli, R.B.G., Paul van Schayck, J., Mykytyn, A.Z., Duimel, H.Q., et al. (2020). SARS-CoV-2 productively infects human gut enterocytes. Science 369, 50–54.

LeBleu, V.S., Taduri, G., O'Connell, J., Teng, Y., Cooke, V.G., Woda, C., Sugimoto, H., and Kalluri, R. (2013). Origin and function of myofibroblasts in kidney fibrosis. Nat. Med. 19, 1047–1053.

Lemos, D.R., McMurdo, M., Karaca, G., Wilflingseder, J., Leaf, I.A., Gupta, N., Miyoshi, T., Susa, K., Johnson, B.G., Soliman, K., et al. (2018). Interleukin-1β activates a MYC-dependent metabolic switch in kidney stromal cells necessary for progressive tubulointerstitial fibrosis. J. Am. Soc. Nephrol. 29, 1690–1705.

Liberzon, A., Birger, C., Thorvaldsdóttir, H., Ghandi, M., Mesirov, J.P., and Tamayo, P. (2015). The Molecular Signatures Database (MSigDB) hallmark gene set collection. Cell Syst. 1, 417–425.

Liberzon, A., Subramanian, A., Pinchback, R., Thorvaldsdóttir, H., Tamayo, P., and Mesirov, J.P. (2011). Molecular signatures database (MSigDB) 3.0. Bioinformatics 27, 1739–1740. https://doi.org/10.1093/bioinformatics/btr260.

Lin, J.Z., Rabhi, N., and Farmer, S.R. (2018). Myocardin-related transcription factor A promotes recruitment of ITGA5+ profibrotic progenitors during obesity-induced adipose tissue fibrosis. Cell Rep. 23, 1977–1987.

Ma, F.Y., Flanc, R.S., Tesch, G.H., Han, Y., Atkins, R.C., Bennett, B.L., Friedman, G.C., Fan, J.H., and Nikolic-Paterson, D.J. (2007). A pathogenic role for c-Jun amino-terminal kinase signaling in renal fibrosis and tubular cell apoptosis. J. Am. Soc. Nephrol. 18, 472–484.

Maarouf, O.H., Aravamudhan, A., Rangarajan, D., Kusaba, T., Zhang, V., Welborn, J., Gauvin, D., Hou, X., Kramann, R., and Humphreys, B.D. (2016). Paracrine Wnt1 drives interstitial fibrosis without inflammation by tubulointerstitial cross-talk. J. Am. Soc. Nephrol. 27, 781–790.

Markó, L., Vigolo, E., Hinze, C., Park, J.K., Roël, G., Balogh, A., Choi, M., Wübken, A., Cording, J., Blasig, I.E., et al. (2016). Tubular epithelial NF-κB activity regulates ischemic AKI. J. Am. Soc. Nephrol. 27, 2658–2669.

McBride, R., van Zyl, M., and Fielding, B.C. (2014). The coronavirus nucleocapsid is a multifunctional protein. Viruses 6, 2991–3018.

Monteil, V., Kwon, H., Prado, P., Hagelkrüys, A., Wimmer, R.A., Stahl, M., Leopoldi, A., Garreta, E., Hurtado Del Pozo, C., Prosper, F., et al. (2020). Inhibition of SARS-CoV-2 infections in engineered human tissues using clinical-grade soluble human ACE2. Cell 181, 905–913.e7.

Müller, J.A., Groß, R., Conzelmann, C., Krüger, J., Merle, U., Steinhart, J., Weil, T., Koepke, L., Bozzo, C.P., Read, C., et al. (2021). SARS-CoV-2 infects and replicates in cells of the human endocrine and exocrine pancreas. Nat. Metab. 3, 149–165.

Muramatsu, T. (2016). Basigin (CD147), a multifunctional transmembrane glycoprotein with various binding partners. J. Biochem. 159, 481–490.

Murgolo, N., Therien, A.G., Howell, B., Klein, D., Koeplinger, K., Lieberman, L.A., Adam, G.C., Flynn, J., McKenna, P., Swaminathan, G., et al. (2021). SARS-CoV-2 tropism, entry, replication, and propagation: considerations for drug discovery and development. PLoS Pathog. 17, e1009225.

Muto, Y., Wilson, P.C., Ledru, N., Wu, H., Dimke, H., Waikar, S.S., and Humphreys, B.D. (2021). Single cell transcriptional and chromatin accessibility profiling redefine cellular heterogeneity in the adult human kidney. Nat. Commun. 12, 2190.

Nagai, J.S., Leimkühler, N.B., Schaub, M.T., Schneider, R.K., and Costa, I.G. (2021). CrossTalkeR: analysis and visualization of ligand–receptor networks. Bioinformatics 37, 4263–4265. https://doi.org/10.1093/bioinformatics/btab370.

Omer, D., Pleniceanu, O., Gnatek, Y., Namestnikov, M., Cohen-Zontag, O., Goldberg, S., Friedman, Y.E., Friedman, N., Mandelboim, M., Vitner, E.B., et al. (2021). Human kidney spheroids and monolayers provide insights into SARS-CoV-2 renal interactions. J. Am. Soc. Nephrol. 32, 2242–2254.

Örd, M., Faustova, I., and Loog, M. (2020). The sequence at Spike S1/S2 site enables cleavage by furin and phospho-regulation in SARS-CoV2 but not in SARS-CoV1 or MERS-CoV. Sci. Rep. 10, 16944.

Pellegrini, L., Albecka, A., Mallery, D.L., Kellner, M.J., Paul, D., Carter, A.P., James, L.C., and Lancaster, M.A. (2020). SARS-CoV-2 infects the brain choroid plexus and disrupts the blood-CSF barrier in human brain organoids. Cell Stem Cell 27, 951–961.e5.

Phipson, B., Er, P.X., Combes, A.N., Forbes, T.A., Howden, S.E., Zappia, L., Yen, H.J., Lawlor, K.T., Hale, L.J., Sun, J., et al. (2019). Evaluation of variability in human kidney organoids. Nat. Methods 16, 79–87.

Piñeiro, G.J., Molina-Andújar, A., Hermida, E., Blasco, M., Quintana, L.F., Rojas, G.M., Mercadal, J., Castro, P., Sandoval, E., Andrea, R., et al. (2021). Severe acute kidney injury in critically ill COVID-19 patients. J. Nephrol. 34, 285–293.

Puelles, V.G., Lütgehetmann, M., Lindenmeyer, M.T., Sperhake, J.P., Wong, M.N., Allweiss, L., Chilla, S., Heinemann, A., Wanner, N., Liu, S., et al. (2020). Multiorgan and renal tropism of SARS-CoV-2. N. Engl. J. Med. 383, 590–592.

Qiu, H., Wander, P., Bernstein, D., and Satapathy, S.K. (2020). Acute on chronic liver failure from novel severe acute respiratory syndrome coronavirus 2 (SARS-CoV-2). Liver Int. 40, 1590–1593.

Rayego-Mateos, S., Rodrigues-Diez, R., Morgado-Pascual, J.L., Valentijn, F., Valdivielso, J.M., Goldschmeding, R., and Ruiz-Ortega, M. (2018). Role of epidermal growth factor receptor (EGFR) and its ligands in kidney inflammation and damage. Mediators Inflamm. 2018, 8739473.

Satija, R., Farrell, J.A., Gennert, D., Schier, A.F., and Regev, A. (2015). Spatial reconstruction of single-cell gene expression data. Nat. Biotechnol. 33, 495–502.

Schell, C., and Huber, T.B. (2017). The evolving complexity of the podocyte cytoskeleton. J. Am. Soc. Nephrol. 28, 3166–3174.

Schraivogel, D., Gschwind, A.R., Milbank, J.H., Leonce, D.R., Jakob, P., Mathur, L., Korbel, J.O., Merten, C.A., Velten, L., and Steinmetz, L.M. (2020). Targeted Perturb-seq enables genome-scale genetic screens in single cells. Nat. Methods 17, 629–635.

Schubert, M., Klinger, B., Klünemann, M., Sieber, A., Uhlitz, F., Sauer, S., Garnett, M.J., Blüthgen, N., and Saez-Rodriguez, J. (2018). Perturbation-response genes reveal signaling footprints in cancer gene expression. Nat. Commun. 9, 20.

Schunk, S.J., Floege, J., Fliser, D., and Speer, T. (2021). WNT-β-catenin signalling - a versatile player in kidney injury and repair. Nat. Rev. Nephrol. 17, 172–184.

Shen, Y., Miao, N., Wang, B., Xu, J., Gan, X., Xu, D., Zhou, L., Xue, H., Zhang, W., Yang, L., and Lu, L. (2017). c-Myc promotes renal fibrosis by inducing integrin αv-mediated transforming growth factor-β signaling. Kidney Int. 92, 888–899.

Soo, J.Y.-C., Jansen, J., Masereeuw, R., and Little, M.H. (2018). Advances in predictive in vitro models of drug-induced nephrotoxicity. Nat. Rev. Nephrol. 14, 378–393.

Takahashi, K., and Yamanaka, S. (2006). Induction of pluripotent stem cells from mouse embryonic and adult fibroblast cultures by defined factors. Cell 126, 663–676.

Takasato, M., Er, P.X., Chiu, H.S., and Little, M.H. (2016). Generation of kidney organoids from human pluripotent stem cells. Nat. Protoc. *11*, 1681–1692.

Takasato, M., Er, P.X., Chiu, H.S., Maier, B., Baillie, G.J., Ferguson, C., Parton, R.G., Wolvetang, E.J., Roost, M.S., Chuva de Sousa Lopes, S.M., and Little, M.H. (2015). Kidney organoids from human iPS cells contain multiple lineages and model human nephrogenesis. Nature *526*, 564–568.

Tammaro, A., Kers, J., Scantlebery, A.M.L., and Florquin, S. (2020). Metabolic flexibility and innate immunity in renal ischemia reperfusion injury: the fine balance Between adaptive repair and tissue degeneration. Front. Immunol. *11*, 1346.

The Human Protein Atlas (2015). Tissue expression of ACE2 - Staining in kidney - the Human Protein Atlas, https://www.proteinatlas.org/ENSG00000130234-ACE2/tissue/kidney.

Triana, S., Stanifer, M.L., Metz-Zumaran, C., Shahraz, M., Mukenhirn, M., Kee, C., Serger, C., Koschny, R., Ordoñez-Rueda, D., Paulsen, M., et al. (2021). Single-cell transcriptomics reveals immune response of intestinal cell types to viral infection. Mol. Syst. Biol. *17*, e9833.

Tsuyuzaki, K., Ishii, M., Nishida, K. (2019). Uncovering hypergraphs of cell-cell interaction from single cell RNA-sequencing data. bioRxiv 566182; https://doi.org/10.1101/566182

Uhlén, M., Fagerberg, L., Hallström, B.M., Lindskog, C., Oksvold, P., Mardinoglu, A., Sivertsson, Å., Kampf, C., Sjöstedt, E., Asplund, A., et al. (2015). Proteomics. Tissue-based map of the human proteome. Science *347*, 1260419.

Varghese, F.S., van Woudenbergh, E., Overheul, G.J., Eleveld, M.J., Kurver, L., van Heerbeek, N., van Laarhoven, A., Miesen, P., den Hartog, G., de Jonge, M.I., and van Rij, R.P. (2021). Berberine and obatoclax inhibit SARS-Cov-2 replication in primary human nasal epithelial cells in vitro. Viruses *13*, 282.

Vento-Tormo, R., Efremova, M., Botting, R.A., Turco, M.Y., Vento-Tormo, M., Meyer, K.B., Park, J.E., Stephenson, E., Polański, K., Goncalves, A., et al. (2018). Single-cell reconstruction of the early maternal-fetal interface in humans. Nature *563*, 347–353. https://doi.org/10.1038/s41586-018-0698-6.

Wang, K., Chen, W., Zhang, Z., Deng, Y., Lian, J.Q., Du, P., Wei, D., Zhang, Y., Sun, X.X., Gong, L., et al. (2020). CD147-spike protein is a novel route for SARS-CoV-2 infection to host cells. Signal Transduct. Target. Ther. *5*, 283.

Wang, Z., Gall, J.M., Bonegio, R.G.B., Havasi, A., Hunt, C.R., Sherman, M.Y., Schwartz, J.H., and Borkan, S.C. (2011). Induction of heat shock protein 70 inhibits ischemic renal injury. Kidney Int. *79*, 861–870.

Wang, Y., Wang, R., Zhang, S., Song, S., Jiang, C., Han, G., Wang, M., Ajani, J., Futreal, A., Wa, L., et al. (2019). iTALK: an R Package to Characterize and Illustrate Intercellular. Communication bioRxiv *507871*. https://doi.org/10.1101/507871.

Wichmann, D., Sperhake, J.P., Lütgehetmann, M., Steurer, S., Edler, C., Heinemann, A., Heinrich, F., Mushumba, H., Kniep, I., Schröder, A.S., et al. (2020). Autopsy findings and venous thromboembolism in patients With COVID-19: A prospective cohort study. Ann. Intern. Med. *173*, 268–277.

Wu, H., Lai, C.F., Chang-Panesso, M., and Humphreys, B.D. (2020). Proximal tubule translational profiling during kidney fibrosis reveals proinflammatory and Long noncoding RNA expression patterns with sexual dimorphism. J. Am. Soc. Nephrol. *31*, 23–38.

Yu, G., Wang, L.G., Han, Y., and He, Q.Y. (2012). clusterProfiler: an R package for comparing biological themes among gene clusters. OMICS *16*, 284–287.

Zang, R., Gomez Castro, M.F., McCune, B.T., Zeng, Q., Rothlauf, P.W., Sonnek, N.M., Liu, Z., Brulois, K.F., Wang, X., Greenberg, H.B., et al. (2020). TMPRSS2 and TMPRSS4 promote SARS-CoV-2 infection of human small intestinal enterocytes. Sci. Immunol. *5*, eabc3582.

Zheng, G.X.Y., Terry, J.M., Belgrader, P., Ryvkin, P., Bent, Z.W., Wilson, R., Ziraldo, S.B., Wheeler, T.D., McDermott, G.P., Zhu, J., et al. (2017). Massively parallel digital transcriptional profiling of single cells. Nat. Commun. *8*, 14049.

Zhou, D., Tan, R.J., Zhou, L., Li, Y., and Liu, Y. (2013). Kidney tubular β-catenin signaling controls interstitial fibroblast fate via epithelial-mesenchymal communication. Sci. Rep. *3*, 1878.

STAR★METHODS

KEY RESOURCES TABLE

REAGENT or RESOURCE	SOURCE	IDENTIFIER
Antibodies		
anti-human ACE2, polyclonal goat IgG	Bio-Techne, UK	Cat#AF933; RRID:AB_355722
anti-human SARS-CoV-2 nucleoprotein, monoclonal mouse IgG1	Sino Biological Europe	Cat#40143-MM05; RRID:AB_2827977
biotinylated lotus tetragonolobus lectin (LTL)	Brunschwig Chemie	Cat#B1325; RRID:AB_2336558
anti-human VE-cadherin, polyclonal goat IgG	Cite ab	Cat#sc-6458; RRID:AB_2077955
anti-human Synaptopodin, monoclonal mouse IgG1	Progen Biotechnik	Cat#61094; RRID:AB_1543006
anti-human Annexin III, polyclonal rabbit IgG	Sigma-Aldrich	Cat#HPAO13398
anti-human Nephrin, polyclonal sheep IgG	R&D Systems	Cat#AF4269; RRID:AB_2154851
anti-human PDGFRa, monoclonal mouse IgG2a	BD Pharmingen	Cat# 556001; RRID:AB_396285
anti-human PDGFRb, monoclonal mouse IgG1	Abcam	Cat# ab69506; RRID:AB_1269704
anti-human Collagen 1, polyclonal rabbit IgG	Abcam	Cat# ab34710; RRID:AB_731684
Alexa Fluor donkey anti-goat IgG 488 (H+L)	Thermo Fisher	Cat#A11055; RRID:AB_2534102
Alexa Fluor donkey anti-mouse IgG 568 (H+L)	Thermo Fisher	Cat#A10037; RRID:AB_2534013
Streptavidin Alexa Fluor 405 conjugate	Thermo Fisher	Cat#S32351
Alexa Fluor donkey anti-rabbit IgG 568 (H+L)	Thermo Fisher	Cat#A10042; RRID:AB_2534017
Alexa Fluor donkey anti-goat IgG 647 (H+L)	Thermo Fisher	Cat#A32849; RRID:AB_2762840
Alexa Fluor donkey anti-mouse IgG 488 (H+L)	Thermo Fisher	Cat#A21202; RRID:AB_141607
Alexa Fluor donkey anti-rabbit IgG 647 (H+L)	Thermo Fisher	Cat#A31573; RRID:AB_2536183
Alexa Fluor donkey anti-sheep IgG 647 (H+L)	Thermo Fisher	Cat#A21448; RRID:AB_10374882
Bacterial and virus strains		
SARS-CoV-2, Bavarian strain	Kindly provided by Christian Drosten, Charité – Universitaetsmedizin Berlin, Germany	GenBank: MT270101.1
Biological samples		
Human COVID-19 patient kidney autopsy tissue Human kidney autopsy control tissue	Radboudumc and UMC Groningen, The Netherlands. RWTH Uniklinik Aachen and UMC Hamburg, Germany. Biobank Erasmus MC Rotterdam, The Netherlands	refer to Table S1
Chemicals, peptides, and recombinant proteins		
Essential 8 FLEX Medium	Thermo Fisher	Cat#A2858501
Essential 6 Medium	Thermo Fisher	Cat#A1516401
UltraPure EDTA (0.5M) pH 8.0	Thermo Fisher	Cat#15575020
Geltrex LDEV-free, hESC-Qualified, reduced growth factor basement membrane matrix	Thermo Fisher	Cat#A1413302
Antibiotic-Antimycotic	Thermo Fisher	Cat#15240062
CHIR 99021	R&D Systems	Cat#4423/10
Recombinant Human FGF-9 Protein	R&D Systems	Cat#273-F9-025
Heparin sodium salt from porcine intestinal mucosa	Sigma-Aldrich	Cat#H4784
Recombinant Human BMP-7 Protein	R&D Systems	Cat#354-BP-010
TrypLE Select Enzyme, no phenol red	Thermo Fisher	Cat#12563-029
SB 431542 hydrate	Sigma-Aldrich	Cat#S4317

(Continued on next page)

Continued

REAGENT or RESOURCE	SOURCE	IDENTIFIER
RevitaCell Supplement	Thermo Fisher	Cat#A2644501
Trypsin-EDTA (0.05%), phenol red	Thermo Fisher	Cat#25300054
Corning® Transwell® polyester membrane cell culture inserts, 24 mm Transwell with 0.4 μm pore polyester membrane insert, TC-treated, sterile	Sigma-Aldrich	Cat#CLS3450
DMEM/F-12	Thermo Fisher	Cat#11320074
human epidermal growth factor	Sigma-Aldrich	Cat#E9644
recombinant Human/Feline CXCL12/SDF1b	R&D Systems	Cat#351-FS-050
[deamino-Cys1, D-Arg8]-Vasopressin acetate salt hydrate, ≥97% (HPLC)	Sigma-Aldrich	Cat#V1005
Aldosterone ≥95% (HPLC)	Sigma-Aldrich	Cat#A9477
Critical commercial assays		
PureLink RNA mini kit	Thermo Fisher	Cat#12183018A
PSC Cryopreservation Kit	Thermo Fisher	Cat#351-FS-050
TaqMan Reverse Transcription kit	Thermo Fisher	Cat#N8080234
RNAscope® Multiplex Fluorescent Reagent Kit v2 assay	Advanced Cell Diagnostics	Cat#323100
RNAscope® 2.5 HD Reagent kit - Brown	Advanced Cell Diagnostics	Cat#322300
RNAscope® probe - V-nCoV2019-orf1ab-sense	Advanced Cell Diagnostics	Cat#859151
RNAscope® probe -V-nCoV2019-S	Advanced Cell Diagnostics	Cat#848561-C1
RNAscope® probe -V-nCoV2019-S-sense	Advanced Cell Diagnostics	Cat#845701-C1
RNAscope® probe -Hs-ACE2-C2	Advanced Cell Diagnostics	Cat#848151-C2
RNAscope® probe -Hs-TMPRSS2-C2	Advanced Cell Diagnostics	Cat#470341-C2
Chromium Next GEM Single Cell 3' Kit v3.1, 16 rxns	10x Genomics	Cat#1000268
Dual Index Kit TT Set A, 96 rxns	10x Genomics	Cat#1000215
Chromium Next GEM Chip G Single Cell Kit, 16 rxns	10x Genomics	Cat#1000127
Library Construction Kit 16 rxns	10x Genomics	Cat#1000190
NovaSeq 6000 S2 Reagent Kit v1.5 (100 cycles)	Illumina	Cat#20028316
MAT-POS-b3e365b9-1	Provided by The COVID Moonshot Consortium	https://covid.postera.ai/covid/submissions/b3e365b9-9ba1-48cb-bc05-132b14d906ad/1
Deposited data		
scRNA- and snRNA-seq data	This paper; deposited on Gene Expression Omnibus (GEO)	https://www.ncbi.nlm.nih.gov/geo/query/acc.cgi?acc=GSE167747
Scripts and codes for data analysis	This paper; deposited on Zenodo	https://zenodo.org/record/5776147
Experimental models: Cell lines		
Human induced pluripotent stem cell line iPS 15	SCTC Radboud UMC, The Netherlands	iPS 15
Vero clone E6	American Type Culture Collection (ATCC)	Cat#CRL-1586
Oligonucleotides		
Human SARS-CoV-2 E protein gene forward primer: 5′-ACAGGTACGTTAATAGTTAATAGCGT-3′	(Corman et al., 2020)	N/A
Human SARS-CoV-2 E protein gene reverse primer: 5′-ACAGGTACGTTAATAGTTAATAGCGT-3′	(Corman et al., 2020)	N/A
Human β-actin gene forward primer: 5′-CCTTCCTGGGCATGGAGTCCTG-3′	Experimental Virology, Radboud UMC, Nijmegen, The Netherlands	This paper

(Continued on next page)

Continued

REAGENT or RESOURCE	SOURCE	IDENTIFIER
Human β-actin gene reverse primer: 5′-GGAGCAATGATCTTGATCTTC-3′	Experimental Virology, Radboud UMC, Nijmegen, The Netherlands	This paper
Software and algorithms		
ImageJ version Fiji 1.51n	National Institutes of Health, USA	https://imagej.nih.gov/ij/
ZEN 3.0 blue edition	Carl Zeiss	https://www.zeiss.de/mikroskopie/produkte/mikroskopsoftware/zen.html
Cell Ranger version 3.1.0	10x genomics	https://support.10xgenomics.com/single-cell-gene-expression/software/release-notes/2-1
Seurat version 3.2.3	Butler et al., 2018	https://satijalab.org/seurat/
R 4.0.3	CRAN	https://www.R-project.org
Adobe InDesign CC2021	Adobe Systems Inc.	https://www.adobe.com/de/products/indesign.html
Adobe Illustrator CC 2021	Adobe Systems Inc.	RRID:SCR_010279
Adobe Photoshop CC 2021	Adobe Systems Inc.	RRID:SCR_014199
GraphPad Prism version 9.0	GraphPad Software Inc.	RRID:SCR_002798
Dragonfly software version 2021.1 for Windows	Object Research Systems (ORS)	http://www.theobjects.com/dragonfly
ClusterProfiler 3.14.3	http://doi.org/10.1089/omi.2011.0118 (Yu et al., 2012)	https://bioconductor.org/packages/release/bioc/html/clusterProfiler.html
PROGENy 1.12.0	https://doi.org/10.1038/s41467-017-02391-6 (Schubert et al., 2018)	https://saezlab.github.io/progeny/
DoRothEA 1.2.0	https://doi.org/10.1158/0008-5472.can-17-1679 (Garcia-Alonso et al., 2018)	https://saezlab.github.io/dorothea/index.html
CrossTalkeR 1.0.2	https://doi.org/10.1101/2021.01.20.427390 (Nagai et al., 2021)	https://github.com/CostaLab/CrossTalkeR
CellPhoneDB 2.0.5	https://doi.org/10.1038/s41586-018-0698-6 (Vento-Tormo et al., 2018)	https://www.cellphonedb.org/
msigdb 7.2.1	https://doi.org/10.1093/bioinformatics/btr260 (Liberzon et al., 2011)	https://cran.r-project.org/web/packages/msigdbr/index.html

RESOURCE AVAILABILITY

Lead contact
Further information and requests for resources and reagents should be directed to and will be fulfilled by the lead contact, Rafael Kramann, MD, PhD (rkramann@gmx.net).

Materials availability
This study did not generate new unique reagents. For specific details on materials availability please refer to the Key resources table.

Data and code availability
Single cell RNA sequencing data generated for this study is available from Gene Expression Omnibus (GEO): https://www.ncbi.nlm.nih.gov/geo/query/acc.cgi?acc=GSE167747. The scripts used for pathway analyses (PROGENy and DoRothEA), ligand-receptor analysis, virus read detection (viral track), as well as the Fiji macro for fibrosis quantification in Masson's trichrome staining are available on Zenodo: https://zenodo.org/record/5776147. Any additional information required to reanalyze the data reported in this paper is available from the lead contact upon request.

EXPERIMENTAL MODEL AND SUBJECT DETAILS

Human autopsy, nephrectomy, and biopsy kidney tissue

COVID-19 human kidney tissues and control tissues were obtained at the Department of Nephrology and Pathology at Radboud University Medical Center in Nijmegen, The Netherlands, the Department of Pathology and Medical Biology at University Medical Center in Groningen, The Netherlands, the III. Department of Medicine of the University Medical Center Hamburg-Eppendorf in Hamburg, Germany, the Department of Pathology at the RWTH University Hospital Aachen, Germany the Institute for Experimental Medicine and Systems Biology of the RWTH University Hospital in Aachen, Germany and the biobank of Erasmus Medical Center in Rotterdam, The Netherlands. Ethics approval numbers: 2018-4086, PV7311, EK 042/17, EK 460/20, EK-016/17.

Human induced pluripotent stem cells (iPSCs)

Human adult skin fibroblasts derived from a healthy volunteer were reprogrammed into iPSCs using the Yamanaka factors (Takahashi and Yamanaka, 2006) by the Stem Cells Technology Center at Radboud University Medical Center (SCTC, Radboud UMC, Nijmegen, The Netherlands). The iPSCs used in the current study were generated from spare materials from a healthy donor, who did consent with the use of such material and did not suffer from kidney disease. The materials have been anonymized and were collected during a time in which no signed informed consent was required.

Culturing human induced pluripotent stem cell (iPSC) derived kidney organoids

iPSC were seeded using a density of 18,000 cells/cm^2 on Geltrex (Thermo Fisher, Breda, the Netherlands) coated 6-well plates (Greiner Bio-one, Alphen aan de Rijn, the Netherlands). The differentiation protocol was based on Takasato et al. with slight modifications (Takasato et al., 2016). On day 0 (d 0), differentiation was initiated using CHIR-99021 (6 μM, R&D systems, Abingdon, United Kingdom) in Essential 6 medium (E6, Thermo Fisher). CHIR treatment was maintained for 3 (differentiation towards ureteric bud) and 5 days (differentiation towards metanephric mesenchyme) and medium was replaced sequentially for E6 supplemented with fibroblast growth factor 9 (FGF9), 200 ng/ml, R&D systems) and heparin (1 μg/ml, Sigma-Aldrich, Zwijndrecht, Netherlands) up to d 7. Cell layers were trypsinized and suspensions were counted on d 7. One part 3 days CHIR-differentiated cells was mixed with two parts 5 days CHIR-differentiated cells. To generate cell aggregates, cells were aliquoted using 300,000 cells per 1.5 ml tube and centrifuged 3 times at 300 rcf for 3 min changing position by 180° per cycle. Cell aggregates were plated on Costar Transwell filters (type 3450, Corning, Sigma-Aldrich) and cultured at an air-medium interface as a 3D organoid model. One-hour CHIR pulse (5 μM) in E6 was used to stimulate self-organizing nephrogenesis and medium was replaced for E6 supplemented with FGF9 and heparin for additional 5 days. As of d 7+5, organoids were cultured using E6 media supplemented with human epidermal growth factor (hEGF, 10 ng/ml, Sigma-Aldrich), bone morphogenetic protein-7 (BMP7, 50 ng/ml, R&D systems), stromal derived factor 1 beta (SDF1β, 10 ng/ml, R&D systems), vasopressin (10 nM, Sigma-Aldrich), aldosterone (10 nM, Sigma-Aldrich) until viral infection at d 7+18.

METHOD DETAILS

RNA extraction, cDNA synthesis and viral load analysis

RNA from organoids was isolated using the PureLink RNA mini kit (Thermo Fisher) according to the manufacturer's protocol. RNA was stored at -80°C until further processing. cDNA was synthesized using the TaqMan Reverse Transcription kit and random hexamers (Applied Biosystems) according to the manufacturer's protocol, using 200 ng RNA as input. Viral RNA load was quantified by performing a semi-quantitative real-time PCR using GoTaq qPCR (Promega) BRYT Green Dye-based kit and primers targeting the SARS-CoV-2 E protein gene. A standard curve of a plasmid containing the E gene qPCR amplicon was used to convert Ct values to relative genome copy numbers after normalization with the corresponding human β-actin gene expression levels. For primer sequences please refer to the key resources table.

Infection of human iPSC-derived kidney organoids with SARS-CoV-2 and treatment with TGFb inhibitor SB431542

SARS-CoV-2 isolate BetaCoV/Munich/BavPat1/2020 (European Virus Archive no. 026V-03883, GenBank: MT270101.1), kindly provided by Christian Drosten (Charité - Universitätsmedizin Berlin, Berlin Institute of Virology, Berlin, Germany), was grown and titered on Vero E6 cells as described previously (Varghese et al., 2021). Organoids were infected with SARS-CoV-2 (BayPat1, GenBank: MT270101.1) in transwell filters (Corning) using a multiplicity of infection (MOI) of 1.0 in E6 medium for 4 h at 37°C, 5% (v/v) CO$_2$ exposing both on top and below the transwell to gain maximum exposure surface area. Medium containing virus was replaced with new medium (no virus) and cultured for an additional 5 days, in the presence or absence of SB431542 (10 μM, Sigma-Aldrich). After 5 days, organoids were washed in PBS, harvested, and processed for further analysis.

Blocking SARS-CoV-2 entry into kidney organoid cells by MAT-POS-b3e365b9-1

For antiviral assays, organoids were infected with SARS-CoV-2 at an MOI of 1.0 in the presence of 10 μM MAT-POS-b3e365b9-1 or 0.1% DMSO. MAT-POS-b3e365b9-1 was designed by the Moonshot initiative, synthesized by Enamine (Ukraine) and provided as 10 mM stocks in DMSO (Chodera et al., 2020; Achdout et al., 2020). Organoids were harvested at 48 and 96 hpi, and supernatants from the apical compartment harvested at 96 hpi, were analyzed by RT-qPCR and plaque assays as described previously (Varghese

et al., 2021). Antiviral activity on Vero E6 cells was tested by inoculating cells at an MOI of 0.01 for 1 h, after which the cells were washed with PBS and treated with a serial dilution of MAT-POS-b3e365b9-1 in DMEM. The supernatant was harvested at 24 hpi for RNA isolation using the QIAamp viral RNA mini kit (Qiagen) and RT-qPCR as described (Varghese et al., 2021). CellTiter-Glo assay (Promega) was used to assess cell viability (in absence of infection).

Preparing paraffin sections of human iPSC-derived kidney organoids
Upon harvesting after SARS-CoV-2 infection, single iPSC-derived kidney organoids were cut from the Transwell filter using a scalpel and fixed in 4% (v/v) formalin for 30 min. Subsequently, fixated kidney organoids were removed from the filter membrane with the help of a scalpel and two organoids from the same condition were merged on top of each other in a cryomold (Tissue-Tek, Sakura Finetek Europe B.V., Alphen aan de Rijn, the Netherlands) in 2.25% (w/v) agarose gel (Thermo Fisher). After gelling for 5 min at 4°C, the agarose-embedded organoid cubes were transferred to embedding cassettes (Paul Marienfeld, Lauda Königshofen, Germany) and paraffinized. After paraffin processing, organoid sections were cut at a thickness of 4 μm using a microtome and mounted on FLEX IHC Microscope Slides (DAKO, Agilent Technologies, Amstelveen, the Netherlands).

Fluorescence In Situ Hybridization (FISH)
3-μm-thick formalin-fixed paraffin sections were deparaffinized in xylene and then dehydrated with 100% ethanol. FISH was performed on the sections with the RNAscope® Multiplex Fluorescent Reagent Kit v2 assay (Advanced Cell Diagnostics, Inc., Hayward, California, USA). Briefly, we incubated the tissue sections with H_2O_2 and performed a heat-induced target retrieval step followed by protease incubation with the reagents provided. RNA sequences of SARS-CoV-2 S gene, SARS-CoV-2 antisense, ACE2 and TMPRSS2 were hybridized using RNAscope® probe -V-nCoV2019-S (#848561-C1), -V-nCoV2019-S-sense (#845701-C1), -Hs-ACE2-C2 (#848151-C2) and -Hs-TMPRSS2-C2 (#470341-C2), respectively. Positive (C1: *POLR2A* gene of *Homo sapiens*; C2: *PPIB* gene of *Homo sapiens*) and negative probes (*dap* gene of *Bacillus subtilis*) were also applied in each experiment. After the amplifier steps according to the manual, Opal™ 570 and 650 fluorophores (PerkinElmer Life and Analytical Sciences, Boston, MA) were applied to the tissues incubated with C1 and C2 probes, respectively. Finally, nuclei were labeled with DAPI and the slides were mounted with ProLong™ Gold antifade reagent (Invitrogen, Waltham, MA). Sections were analyzed with Zeiss Axio Imager 2 and image analysis software (ZEN 3.0 blue edition).

RNAscope 2.5 High Definition (HD) - BROWN Assay In Situ Hybridization
In situ hybridization (RNAscope technology, Advanced Cell Diagnostics, Inc., Newark, CA, USA) was performed on 4 μm FFPE organoid sections adhered to SuperFrost PLUS microscope slides in order to detect SARS-CoV-2 genomic RNA and virus replication. The RNAscope 2.5 High Definition (HD) - BROWN Assay was used according to the manufacturer's instructions. Briefly, freshly cut sections (<24 h) were deparaffinized in fresh xylene and fresh 100% ethanol and then air dried. Target retrieval was performed (RNAscope® Target Retrieval Reagents, Advanced Cell Diagnostics) following treatment with H_2O_2 (blockage of endogenous peroxidase activity) after which sections were treated with protease (RNAscope® H202 & Protease Plus Reagents, Advanced Cell Diagnostics). Probes specific for SARS-CoV-2 S gene encoding the spike protein (RNAscope® Probe - V-nCoV2019-S, Advanced Cell Diagnostics) and SARS-CoV-2, antisense strand of the orf1ab gene (RNAscope® Probe - V-nCoV2019-orf1ab-sense, Advanced Cell Diagnostics) were incubated on slides to detect SARS-CoV-2 genomic RNA and replicating virus, respectively. Hybridized probes were detected using a diaminobenzidine (DAB)-based assay (RNAscope® 2.5 HD Detection Reagent-BROWN, Advanced Cell Diagnostics). Finally, slides were stained with 50% hematoxylin solution, rinsed with ammonia water, dehydrated and mounted. Slides were digitally scanned using a Hamamatsu Nanozoomer 2.0HT (Hamamatsu Photonics, Hamamatsu, Japan).

Immunofluorescence staining
Paraffin slides were deparaffinized using xylol and ethanol ranges. Tris-buffered EDTA antigen retrieval was performed using boiling for 10 min. All primary (1:100) and secondary (1:200) antibodies were diluted in PBS + 1% (v/v) bovine serum albumin (BSA, VWR). Primary antibodies were incubated overnight at 4°C, secondary antibodies 2 h at room temperature. After antibody incubations, sections were washed 3x with PBS. Slices were mounted in Fluoromount-G® (Southern Biotech, Sanbio, Uden, the Netherlands). For details about primary and matching secondary antibodies used refer to the key resources table.

Immuno-based correlative light microscopy and electron microscopy (CLEM)
Whole mount organoid staining
Whole mount staining was performed according to an adapted protocol based on *Takasato et al.* (Takasato et al., 2015). Briefly, organoids were trimmed and fixed using 0.1% (v/v) glutaraldehyde in 4% (w/v) PFA at 4°C for 45 minutes. After PBS wash, organoids were blocked in a blocking buffer containing 10% (v/v) donkey serum (GeneTex, Irvine, California) in PBS at room temperature for 2h. In contrast to Takasato et al, no Triton-X was added to the blocking buffer to preserve ultrastructure analysis. Primary antibodies (NPHS1, RD systems, catnr AF4269; LTL, VectorLabs, catnr B1325; SARS-CoV-2 nucleocapsid protein, SinoBiological, catnr 40143-MM05) were diluted 1:100 in blocking buffer and incubated at 4°C for 72h. Next, organoids were washed using PBS. Secondary antibodies (donkey a-sheep IgG (H+L) Alexa Fluor 647, Streptavidin Alexa Fluor 405, donkey a-mouse IgG (H+L) Alexa Fluor 488), were diluted 1:200 in PBS and incubated at 4°C for 24h. Next, organoids were washed using PBS. Organoid samples were imaged using a LSM 900 confocal microscope (Carl Zeiss) to locate regions of interest prior to high pressure freezing (HPF).

High pressure freezing and freeze substitution

Parts of the organoid samples were immersed in 10% (v/v) dextran (31389, Sigma) and sandwiched between HPF carriers with 2 mm interior diameter (type A (0.2 mm cavity)), and type B flat side (0.3mm), Art. 241 and 242, Wohlwend). The flat sides of the carriers were treated with 1% L-α-phosphatidylcholine (61755, Sigma) in ethanol (1.00983.1000, Supelco). The samples were then high pressure frozen using live μ (CryoCapCell) and stored in liquid nitrogen until freeze substitution as described previously (Heiligenstein et al., 2021). For embedding in R221 resin (CryoCapCell), the frozen organoids were transferred to a pre-cooled (-90°C) freeze substitution machine (AFS2, Leica). After the removal of the flat carrier, the 0.2mm carriers with the frozen samples were then placed into a rosette filled with freeze substitution cocktail (0.05% (v/v) uranyl acetate (22400, EMS), 5% (v/v) water in acetone (69030/Z, Tendo's)). The complete freeze substitution protocol is described in Table S5, according to the manufacturer's protocol.

Fluorescence imaging of plastic embedded organoids

The polymerized blocks were imaged with an uptight LSM 900 confocal microscope (Zeiss) to localize COVID positive cells (C Epiplan-Apochromat 10x/0.4 DIC; Plan-Apochromat 63x/1.4 oil DIC). The depth of the cell of interest was measured with the LSM microscopy and the block surface was trimmed accordingly using an UCT ultramicrotome (Leica). Ultrathin sections of ~100 nm thickness were collected on ~15 nm formvar and 1 nm Carbon 100 mesh Cu grids (FCF100-CU-TA, EMS). For fluorescent imaging of the organoid sections on the TEM grids, the grids were placed between a microscopy slide and a coverslip and imaged directly after sectioning. To improve re-localizing the area of interest, a reflection image was added to visualize the localization of the cell of interest in relation to the center of the grid.

Transmission Electron microscopy

Prior TEM imaging, the grids were contrasted for 45 minutes 1% uranyl acetate and for 7 minutes 3% Lead citrate (Ultrostain II, Leica) using an automatic contrasting instrument (AC20, Leica). Transmission electron microscopy images were recorded using a JEOL JEM 1400, at 60 kV. COVID-19 positive cells were located by correlating their location position on the grid based on fluorescent images and reflection images to the location in the electron microscope.

3D focused ion beam - scanning electron microscopy (FIB-SEM)

3D FIB/SEM was performed using a Zeiss Crossbeam 550, and Atlas 5 software. After identification of the region of interest in the FIB/SEM using ZEN Connect (Zeiss), the polymerized blocks were covered with a gold layer to reduce charging (Scancoat SIX, Edwards) and introduced back into the FIB/SEM. As viewing channel for SEM observation, an initial 30 μm wide FIB trench was milled using a FIB probe of 30 kV@15 nA, followed by fine FIB milling using the 30kV@1,5nA probe. For serial FIB milling and SEM imaging, a slice width of 5 nm was chosen, using a probe of 30 kV@700pA. After removal of each slice, Inlens Secondary Electrons (SE) and back-scattered electron (EsB) images of the freshly exposed cross-sections were taken simultaneously at an acceleration potential of 1.5 kV. The EsB grid was set to −1200V. Image voxel size was set to 5 × 5 × 5 nm. After alignment and cropping, a data set of 351 serial sections comprising a volume of X = 7.120 μm, Y = 5.005 μm, Z = 1.755 μm, was obtained.

To enhance contrast, image post processing was done using Matlab. The 3D segmentation images were generated using Dragonfly software, Version 2021.1 for Windows (Object Research Systems (ORS) Inc, Montreal, Canada, 2020; software available at http://www.theobjects.com/dragonfly).

Preparation of single cell suspensions from iPSC-derived kidney organoids

After completion of the 5 d incubation post SARS-CoV-2 infection, organoids were harvested for single cell sequencing. Organoids were first digested in the respective Costar Transwell filters using 300 μl Accutase (Sigma-Aldrich) per well for 15 min. at 37°C. DMEM/F12 medium (Sigma-Aldrich) containing 10% (v/v) FCS (Merck Millipore, Darmstadt, Germany) was added to inactivate Accutase, the cell suspension was filtered through a 40 μm cell strainer (Corning) and spun down at 250xg at room temperature for 5 min. This step was repeated once more to obtain single cell suspensions and reduce background. After the final centrifugation cells were resuspended in PBS (Sigma-Aldrich) containing 0.04% (v/v) BSA (VWR, Darmstadt, Germany) and counted using a Neubauer counting chamber (Carl Roth, Karlsruhe, Germany). A total of eight separate kidney organoids were pooled in one sample. Two mock-infected control samples and two SARS-CoV-2-infected samples were used as input for scRNAseq.

Preparation of single nuclei suspensions from snap-frozen human autopsy kidney tissue

Snap-frozen COVID-19 patient autopsy kidney tissue was obtained from the pathology department at Radboud UMC Nijmegen, the Netherlands. A small piece of kidney tissue (ca. 2x2x2 mm) was thawed in PBS and crushed using a glass douncer and tube (Duran Wheaton Kimble Life Sciences, Wertheim/Main, Germany). After passing the single cell suspension through a 70 μm cell strainer (Greiner), the suspension was centrifuged at 4°C and 300xg for 5 min. Subsequently, the supernatant was discarded and the cell pellet was resuspended in Nuc101 cell lysis buffer supplemented with RNase and protease inhibitors (Recombinant RNase Inhibitor and Superase RNase Inhibitor, Thermo Fisher, and cOmplete Protease Inhibitor, Roche) incubated for one minute and centrifuged at 4°C and 500xg for 5 min. After discarding the supernatant, the nuclei were carefully resuspended in PBS containing 1% (v/v) Ultra-Pure BSA (Invitrogen Ambion, Thermo Fisher) and Protector RNAse inhibitor (Sigma Aldrich), counted, and used in the usual single cell RNA sequencing workflow (10x genomics, v3.1).

Single cell and single nuclei RNA library preparation and sequencing

Directly after obtaining single cell or nuclei suspensions, 1000 cells or nuclei/µl per sample were loaded onto a 10x Chromium Next GEM Chip G following the manufacturer's instructions and processed in a Chromium controller (both 10x Genomics, Pleasanton, USA). All single cell and nuclei sequencing libraries were generated using 10x Chromium Next GEM v3.1 kits (10x Genomics). Single cell sequencing of the kidney organoid samples was performed on a Novaseq6000 system (Illumina, San Diego, USA), using an S2 v1.5 100 cycles flow cell (Illumina) with run settings 28-10-10-90 cycles. Single nuclei sequencing of the COVID-19 patient kidney autopsy tissue was performed on a NextSeq 500 system (Illumina) using a NextSeq 500/550 High Output Kit v2.5 with 150 cycles capacity (Illumina) with run settings 28-91-8-0. scRNA-seq was performed at Erasmus MC, dept. of Internal Medicine, Nephrology and Transplantation, Rotterdam, The Netherlands. snRNA-seq was done at the IZKF at RWTH Aachen, Germany.

Single nuclei RNA seq data analysis of human autopsy kidney tissue

The autopsy single nucleus raw data were processed using CellRanger (v. 6.0.2) with a human genome (GRCh38) as a reference genome. Next, the CellRanger outputs were processed using the package Seurat scRNAseq downstream analysis (Satija et al., 2015). Next, the proportion of ribosomal, mitochondrial, UMI counts and cell cycle were regressed out and the read counts were log-normalized by using Seurat functions. The resulting data were annotated and integrated using a previously described single nuclei RNA sequenced data set (Muto et al., 2021).

TAP-Seq single nuclei RNA seq data analysis of human autopsy kidney tissue

The Targeted scRNAseq pre-processing was done as described in (Schraivogel et al., 2020; Triana et al., 2021). The demultiplexing per sample followed the Drop-seq tools workflow using the STAR alignment tool. The potential multi-mapping issues were handled by using a custom reference containing only the SARS-CoV-2 genome in the alignment step. The UMI records were retrieved using the GatherMolecularBarcodeDistributionByGene program from Drop-Seq. A custom script was used to filter chimeric reads with a transcript-per-transcript cut-off of 0.25, the UMI records were converted to a feature count. In the overall analysis only the barcodes kept in the single nuclei sequencing were considered, the remaining cells were considered as empty droplets. Additionally, SoupX was used to correct the viral contamination.

Single cell RNA seq data analysis of human iPSC-derived kidney organoids

To align the organoid reads to the human genome GRCh38 and detect the cells, we used Cell Ranger (v. 3.1.0 (Zheng et al., 2017)) with default settings. In the following step, Seurat (v. 3.2.2) was used to perform scRNAseq high level analysis (Satija et al., 2015). Next, the proportion of ribosomal, mitochondrial, UMI counts and cell cycle were regressed out and the read counts were log-normalized by using Seurat functions. The control samples (control 1 and control 2) were integrated with SARS-CoV-2-infected samples (SARS-CoV-2 1 and SARS-CoV-2 2) by using canonical correlation analysis (CCA) based on the first 20 CCs and no scaling (Butler et al., 2018). In a cell type identification step, unsupervised clustering was performed selecting k-shared nearest neighbors to assemble the graph and a resolution of 0.5 and k=12 was adopted. We applied Find Markers to find cluster gene markers. Here, markers with an adjusted p-value > 0.05 were disregarded.

SARS-CoV-2 differential gene expression analysis

Differential gene expression (DGE) analysis was done by using distincts phenotypes by Seurat *FindMarkers*. For each cell type DE genes were selected regarding the adjusted p-value (adjusted p-values < 0.05 and abs. fold change greater than 0.25) and separated in upregulated and downregulated genes based on respective log-FoldChange signals. GO and pathway (KEGG) enrichment analysis were based on *clusterProfiler* (Version 3.14.3;(Yu et al., 2012)) and MSigDB enrichment analysis was done with Hallmark gene sets from *msigdbr* package (Version 7.2.1,(Liberzon et al., 2015)).

SARS-CoV-2 pathway activity and transcription factor analysis

To identify pathway activity related to the phenotypes, PROGENy (Version 1.12.0; (Garcia-Alonso et al., 2019; Schubert et al., 2018)) was used. With this, the activity of 14 pathways was predicted using the top 500 most responsive genes as shown in a benchmark paper (Garcia-Alonso et al., 2019). Pathway activity differences were addressed by Wilcox rank sum test over relevant pathways and cell types (FDR < 5%). Together, the transcription factors (TF) were retrieved by using *msviper* (minsize=2)(Alvarez et al., 2016) using the DoRothEA regulons (confidence levels A,B and C) (Version 1.2.0; (Garcia-Alonso et al., 2018)). To perform the TF activity inference, the DE genes described above were considered, and the TF shared by kidney cells (Loop of Henle Progenitors, Podocytes, and Proximal Tubule Cells) and Mesenchyme 1 and -2 were visualized in a heatmap generated by *pheatmap* R library (Kolde and Kolde, 2015).

Cellular crosstalk

The cellular crosstalk related ligand receptor (LR) inference was done by CellPhoneDB (CPDB, Version 2.0.5; (Efremova et al., 2020)) for each phenotype. scRNA-seq matrices were log-normalized and scaled using Seurat functions. Following, CPDB was performed in a 'statistical_analysis' mode. To increase the reliability of LR inference CPDB input contained a database elaborated by the combination of five LR data sources (CPDB (Efremova et al., 2020), TalkLR(Wang et al., 2020), scTensor (Tsuyuzaki et al., 2019), SCA (Cabello-Aguilar et al., 2020), and iTALK (Wang et al., 2019)), interactions that presented at least two consensus data sources

were kept in the final LR database. Using the statistically significant interactions (p-value<0.05) from CPDB output, ranking and the visualization were generated by CrossTalkeR (v 1.0.0; https://github.com/CostaLab/CrossTalkeR, (Nagai et al., 2021)).

Discovering viral reads using Viral-Track

The detection of SARS-CoV-2 reads from human iPSC-derived kidney organoids was done using the Viral-Track tool (committed version from 14 August 2020 (Bost et al., 2020). The tool is composed of four main steps, which were adapted and described next. First, we merged the SARS-CoV-2 genome (MT270101.1) with the GRCh38 human reference genome and pre-processed the data using UMI-tools as described in the original paper. Second, we performed the quality check and filtering step using the *viral_track_scanning* step (minimal_read_mapped=50). Third, the *viral_track_assembly* was used over the hybrid reference to address the viral genome assembly. Last, the reads were demultiplexed and aligned using the *viral_track_demultiplexing* script. The viral read counts of each cell were combined with the Seurat gene count matrix.

Gene expression analysis of SARS-CoV-2-infected cells

To address the differences between virus infected cells and healthy cells, we divided the SARS-CoV-2-infected samples in two classes, viral reads contaminated cells and healthy cells. Following, the groups were compared using Seurat FindMarkers. We considered all genes with abs. FC > 0.25. GO and KEGG enrichment analyses were done as before. Also, MSigDB enrichment analysis was done by obtaining the hallmark (H) and immunological (C7) gene sets from *msigdbr* package (Version 7.2.1, (Liberzon et al., 2015)).

QUANTIFICATIONS AND STATISTICAL ANALYSIS

Histochemical quantification of collagen

61 COVID-19 patient autopsy kidney tissues and one COVID-19 patient kidney biopsy, and 57 control nephrectomy and influenza/ ARDS patient kidney specimens (Table S1) were Masson's Trichrome stained. To quantify collagen disposition in the interstitial space, a macro, as shown below, was used in Fiji. Five random cortex areas per slide were selected and measured. The mean intensity per slide was plotted. COVID-19 tissue versus nephrectomy tissue was analyzed for statistical analysis.

Quantification of fibrosis within Masson's Trichrome staining in human tissue

Images of 5 random areas in the cortex were captured per patient or control sample using a VisionTek Digital Microscope (Sakura FineTek, Japan). Samples were blinded while capturing images. For the quantification of fibrosis in Masson's Trichrome staining, we applied the following macro in ImageJ (for version details please refer to the key resources table). The macro code is available on our repository on Zenodo as described in the data and code availability section. The mean intensity of the images per sample was used as one data point and plotted.

Fibrosis scoring following Masson's Trichrome staining of SARS-CoV-2-infected kidney organoids

Double-blinded interstitial fibrosis scoring was performed of 4 independent organoid batches, 2 biological replicates per condition, Masson's Trichrome stained, to quantify fibrosis in SARS-CoV-2 infected kidney organoids. Slides showing 70 ± 10 % nephron segments and 30 ± 10 % stromal cells were scored. Scoring grades: 0 = no fibrosis, 1 = mild fibrosis, 2 = moderate fibrosis, 3 = severe fibrosis. SARS-CoV-2-infected organoids versus mock-treated organoids were assessed for statistical analysis.

Quantification of SARS-CoV-2 nucleocapsid protein expression in kidney organoids

The number of podocyte clusters and proximal tubules expressing SARS-CoV-2 nucleocapsid protein were manually scored to quantify the percentage of infected cells. At least 80 podocyte clusters (nephrin positive) and proximal tubules (LTL positive) per slide were scored and analysed 3 independent experiments each performed with 2 biological replicates were included in the analysis.

Statistical analysis

All data are expressed as mean ± SD of three independent experiments, unless stated otherwise. Statistical analysis was performed using one-way ANOVA analysis followed by Tukey post-test or, when appropriate, an unpaired *t* test with GraphPad Prism version 9.0 (La Jolla, CA).